OXFORD

Journal of Petrology, 2022, **63**, 1–32
https://doi.org/10.1093/petrology/egac037
Advance access publication date 16 April 2022
Original Manuscript

Quaternary Collision-Zone Magmatism of the Greater Caucasus

Samuel Bewick[1], Ian J. Parkinson[2], Nigel Harris[1,*], Shota Adamia[3], Nino Sadradze[3], Mark B. Allen[4] and Sam Hammond[1]

[1]School of Environment, Earth and Ecosystem Sciences, Open University, Milton Keynes MK7 6AA, UK
[2]School of Earth Science, University of Bristol, Queens Road, Bristol, BS8 1RJ, UK
[3]Institute of Geophysics, Tbilisi State University, 1/1M. Alexidze Street, 0171, Tbilisi, Georgia
[4]Department of Earth Sciences, Durham University, Durham DH1 3LE, UK
*Corresponding author. School of Environment, Earth and Ecosystem Sciences, Open University, Milton Keynes MK7 6AA, UK. Tel: +44 01908-655171. E-mail: n.b.w.harris@open.ac.uk

Abstract

The Greater Caucasus mountains (Cavcasioni) mark the northern margin of the Arabia–Eurasia collision zone. Magmatism in the central part of the Greater Caucasus began in the Pleistocene, up to ~25 Myr after initial collision. This paper presents bulk-rock and Sr–Nd–Pb isotope geochemistry from 39 Quaternary volcanic rock samples (<450 Ka) recovered from the Mt. Kazbek (Kasbegui) region of the Greater Caucasus, Georgia, to assess the sources and magmatic evolution of these lavas and the possible triggers for melting in the context of their regional tectonics. Compositions are dominantly calc-alkaline basaltic andesite to dacite (57–67 wt % SiO_2). Although the lavas were erupted through thick continental crust, there is little evidence for extensive modification by crustal contamination. Trace element and isotopic systematics indicate that the lavas have supra-subduction zone signatures, most likely reflecting derivation from a lithospheric source that had been modified by melts and/or fluids from material subducted before and during the collisional event. Mass-balance modelling of the Sr–Nd isotope data indicates that the lavas require significant input from a subducted slab, with deep-sourced fluids fluxing the slab into the source region. In contrast with published data from Lesser Caucasus magmatism, data from the Mt. Kazbek region suggest that a compositionally distinct sediment source resides beneath the Greater Caucasus, producing characteristic trace element and Pb isotopic signatures. Two distinct compositional groups and therefore primary liquids can be discerned from the various volcanic centres, both derived from light rare-earth element enriched sources, but with distinct differences in Th/Yb and Dy/Yb ratios and Pb isotopes. Rare-earth element modelling of the lava sources is consistent with 3–4% melting starting in the garnet peridotite and continuing into the spinel facies or, potentially, sited in the garnet-spinel transition zone. Small-scale convection related to mantle upwelling provides a plausible mechanism for Greater Caucasus magmatism and explains the random aspect to the distribution of magmatism across the Arabia–Eurasia collision zone.

Keywords: rare Earth elements, Sr–Nd–Pb isotopes, collision zone, Caucasus

INTRODUCTION

Magmatism is a common feature of continental collision zones, but its origins and significance are not easily understood (Pearce *et al.*, 1990; Guo & Wilson, 2019). Unlike supra-subduction zone magmatism, there is no generally agreed mechanism for the generation of magmatism that takes place after the initial collision between two continents, during ongoing convergence. The common description of 'post-collisional' magmatism is potentially misleading, because continental collision is a long-term process that may take place over tens of millions of years. The two main active continental collisions on Earth are between India and Eurasia and Arabia and Eurasia (Jackson & McKenzie, 1984; Hatzfeld & Molnar, 2010). The chemistry of the syn-collision volcanic rocks in these collision zones can constrain the nature of the crust and mantle beneath them and also provides insights into the processes that generate the magmatism, thereby increasing our understanding of collision zone processes in general.

Young magmatism is a distinctive feature of the Arabia–Eurasia collision zone and is widespread across the northern (Eurasian) side of the original suture (Adamia *et al.*, 2010, 2017; Chiu *et al.*, 2017; Kaislaniemi *et al.*, 2014; Lebedev *et al.*, 2014). Regardless of the exact age of initial collision (see below), Greater Caucasus magmatism postdates the final subduction of the Tethyan Ocean by probably as much as 25–35 Myr.

Volcanism in the Greater Caucasus is well documented (e.g. Lebedev & Vashakidze, 2014), with volcanism in the western part of the Greater Caucasus range predominantly silicic compared to that in the central part of the

Received: September 25, 2021. **Revised:** April 11, 2022. **Accepted:** April 11, 2022

range where there is a wider range of compositions. Most published models for melt generation in the Greater Caucasus require some amount of crustal input. Lebedev *et al.* (2014) suggest there is a common Caucasus mantle composition that is represented by trachy-basalts similar to oceanic island basalts (OIB) erupted in central Georgia, such that intermediate composition rocks from the central range of the Greater Caucasus have undergone small amounts of crustal assimilation (e.g. Parfenov *et al.*, 2019), whereas the silicic volcanics of the western range require significant (50%) crustal assimilation (e.g. Lebedev *et al.*, 2010). By contrast, Bindeman *et al.* (2021) suggest some of the silicic melts of the western Greater Caucasus represent deep crustal melts mixing with subduction-zone derived mantle melts. Recent publications focused on the geochemistry of the much more widely distributed volcanics from the Lesser Caucasus (e.g. Neill *et al.*, 2013, 2015; Adamia *et al.*, 2017; Sugden *et al.*, 2019; Sugden *et al.*, 2020) have all postulated melt generation models that require the melting of a subduction-zone enriched lithospheric source, which may result from prior subduction of the Tethyan slab beneath the Eurasian continental margin (Neill *et al.*, 2013, 2015; Sokól *et al.*, 2018; Sugden *et al.*, 2019). The work by Sugden *et al.* (2020) suggests that some of the geochemical features of this modified lithosphere, such as an enriched sediment melt/fluid signature, have been preserved for >40 Ma and explain some of the similarities in geochemistry of recent volcanics across the entire collision zone. This paper provides new bulk-rock and Sr–Nd–Pb isotope chemistry data for Quaternary volcanic rocks from the central part of the Greater Caucasus range (Fig. 1), with the aim of improving our understanding of the processes that generate magmatic rocks during and following continental collision in general and this part of the Arabia–Eurasia collision zone in particular. Key issues include whether the young Greater Caucasus magmatism is produced by processes common to the more widespread magmatism of the entire collision zone, whether regional magmatism shares similar lithospheric sources and whether Greater Caucasus magmatism should be regarded as a special case, e.g. with origins related to a separate subduction system or post-subduction process.

GEOLOGICAL SETTING

Regional geology

The Greater Caucasus (Fig. 1) is an asymmetric, south-vergent, late Cenozoic fold-and-thrust belt (Adamia *et al.*, 2011) that reaches from the northeast side of the Black Sea to the junction between the South Caspian and Middle Caspian basins. The easternmost segment of the orogen is characterised by a doubly-vergent structure (Mosar *et al.*, 2010; Forte *et al.*, 2014). Foreland basins have developed on both sides of the orogen (Ershov *et al.*, 2003; Adamia *et al.*, 2010, 2011, 2017; Mosar *et al.*, 2010). The structure is highly asymmetrical, with a gentle monocline to the north, and major north-dipping thrusts on the south side of the range, including the Main Caucasus Thrust. Crust in the region is significantly thickened, to ~50–60 km (Philip *et al.*, 1989; Adamia *et al.*, 2011, 2017). Late Cenozoic deformation is a consequence of the Arabia–Eurasia collision (Allen *et al.*, 2004; Sosson *et al.*, 2017). During the collision, the thrust front has migrated southwards into the Kura Basin, and Kura fold and thrust belt (Mosar *et al.*, 2010), which lie in the Transcaucasus that separates the Greater from the Lesser Caucasus to the south (Adamia *et al.*, 2011).

The structure of the Greater Caucasus varies significantly along strike. Basement is exposed in the centre of the range, where Palaeozoic metamorphic and igneous complexes crop out. Active convergence rates across the Greater Caucasus increase eastwards to ~12 mm yr^{-1} (Reilinger *et al.*, 2006). Recent volcanism is present in the west at Mt. Elbrus and in the central part of the range, which includes the volcanic centres that are the focus of this study in the region of Mt. Kazbek (Kezbegui). Pliocene–Pleistocene (2–3 Ma) ignimbrites and associated granites are found at Chegem and Tyrnyauz, to the east of Mt. Elbrus, although no recent plutonic rocks are exposed at Mt. Elbrus or Mt. Kazbek. Seismicity studies (Mellors *et al.*, 2012; Mumladze *et al.*, 2015) report rare sub-crustal (>50 km) earthquakes, up to a depth of 158 ± 4 km, beneath the eastern Greater Caucasus; these events have been interpreted as recording the presence of a slab of oceanic lithosphere beneath the region (Mumladze *et al.*, 2015). By contrast, deep (>150 km), high-velocity seismic anomalies have been interpreted as evidence for lithospheric delamination (Koulakov *et al.*, 2012).

A widely recognised model for the pre-collision history of the Greater Caucasus is that it represents a Paleozoic–Mesozoic–Early Cenozoic back-arc basin (Adamia *et al.*, 2011), developed north of a contemporary arc that is exposed in the Transcaucasus–Lesser Caucasus to the south (Adamia *et al.*, 1981; Saintot *et al.*, 2006). Continental basement exposed in the west of the Greater Caucasus shows Palaeozoic age ranges, indicating affinities with the juvenile crust of the Scythian and Turan platforms to the north and east (Natal'in & Şengör, 2005; Allen *et al.*, 2006). Jurassic basalts within the interior of the Greater Caucasus have been interpreted as the products of a narrow, obliquely extensional oceanic basin (Adamia *et al.*, 1981), similar to the modern Gulf of California (Şengör, 1990). In this model, the original arc/back-arc transition lies under the Rioni and Kura basins between the two modern ranges, while the high peaks, thickened crust and active thrusts of the Greater Caucasus represent strong inversion of this Palaeozoic–Early Cenozoic back-arc basin during the Arabia–Eurasia collision. Initial uplift of the western Greater Caucasus by the Early Oligocene has been interpreted as an early effect of this collision (Dercourt *et al.*, 1986; Vincent *et al.*, 2007) and as marking the end of a period of oceanic subduction in the late Mesozoic and early Cenozoic. Oceanic crustal basement beneath the South Caspian and Black Sea basins represents separate back-arcs, which also developed to

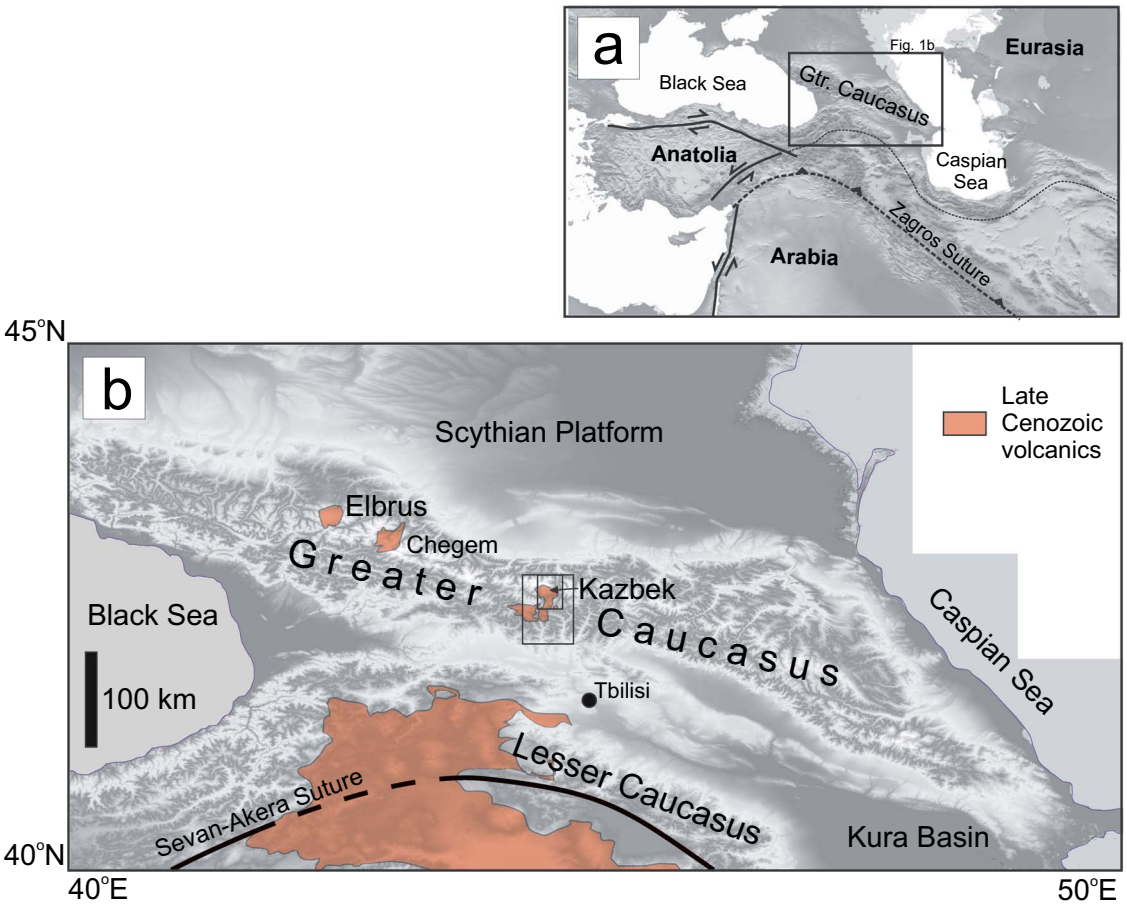

Fig. 1. (a) Location of the Greater Causasus region in the Eurasia–Arabian collision zone, with simplified regional terranes and major tectonics features. (b) Location of Late Cenozoic volcanism in the Caucasus, which includes recent volcanism in the southern Lesser Caucasus that straddles the Georgian/Armenia border and volcanic centres in the northern Greater Causasus that include Mt. Elbrus, Chegem and the area of study, Mt. Kazbek.

the north of the Neo-Tethyan subduction zone (Adamia *et al.*, 1981, 2011, 2017; Okay *et al.*, 1994; Brunet *et al.*, 2003).

Timing of initial collision between Arabia and Eurasia is debated (e.g. Sosson *et al.*, 2010; Adamia *et al.*, 2017), but most estimates place initial collision between ~34 Ma and ~26 Ma (Allen & Armstrong, 2008; Koshnaw *et al.*, 2019). The former age is the time of a sharp reduction in arc and back-arc magmatism across SW Eurasia and the development of unconformities on both sides of the suture (Perotti *et al.*, 2016). The later age is derived from the youngest detrital zircons found within syn-collisional foreland basin strata on the Arabian Plate, within northern Iraq: this represents a minimum age for initial collision. Convergence has continued since initial collision, with the present rate across the collision zone being 16–26 mm yr^{-1}, increasing eastwards due to the pole of rotation lying close to the eastern Mediterranean (Vernant *et al.*, 2004).

There is an alternative model proposed for the Caucasus region (Cowgill *et al.*, 2016), which proposes a wider (oceanic) basin between the Greater and Lesser Caucasus that existed until as recently as ~5 Ma, at which point it was eliminated by subduction northwards under the Greater Caucasus range. This model is disputed (e.g. Adamia *et al.*, 2017; Vincent *et al.*, 2018; Ismail Zadeh *et al.*, 2020), not least because of the lack of a late Cenozoic arc in the Greater Caucasus, and the absence of ophiolites or other clear evidence of a suture zone between the two ranges.

There has been at least sporadic magmatism across the collision zone since the mid-Cenozoic, but with an apparent upsurge in the past ~5 million years (Kaislaniemi *et al.*, 2014). Late Cenozoic magmatism in the Greater Caucasus is concentrated close to the stratovolcano of Mt. Elbrus, the magmatic centres of Chegem and Tyrnyauz (all located within Russia) and the stratovolcano of Mt. Kazbek (on the Georgia–Russia border), which is the focus of this study (Fig. 1b).

Quaternary magmatism in the greater Caucasus of Georgia

Quaternary volcanism in the Greater Caucasus in Georgia is located close to the Russian border, near the towns of Gudauri and Stepantsminda, either side of the Tergi River valley, and in the Keli Highland (Fig. 2). The region consists of the areas of Mt. Kazbek, Gudauri, Qabarjina and the Keli Highland that we sampled during a field season in 2013. Volcanism in the region displays a wide range of volcanic styles, from explosive volcanoclastic deposits to thick columnar jointed flows that can be

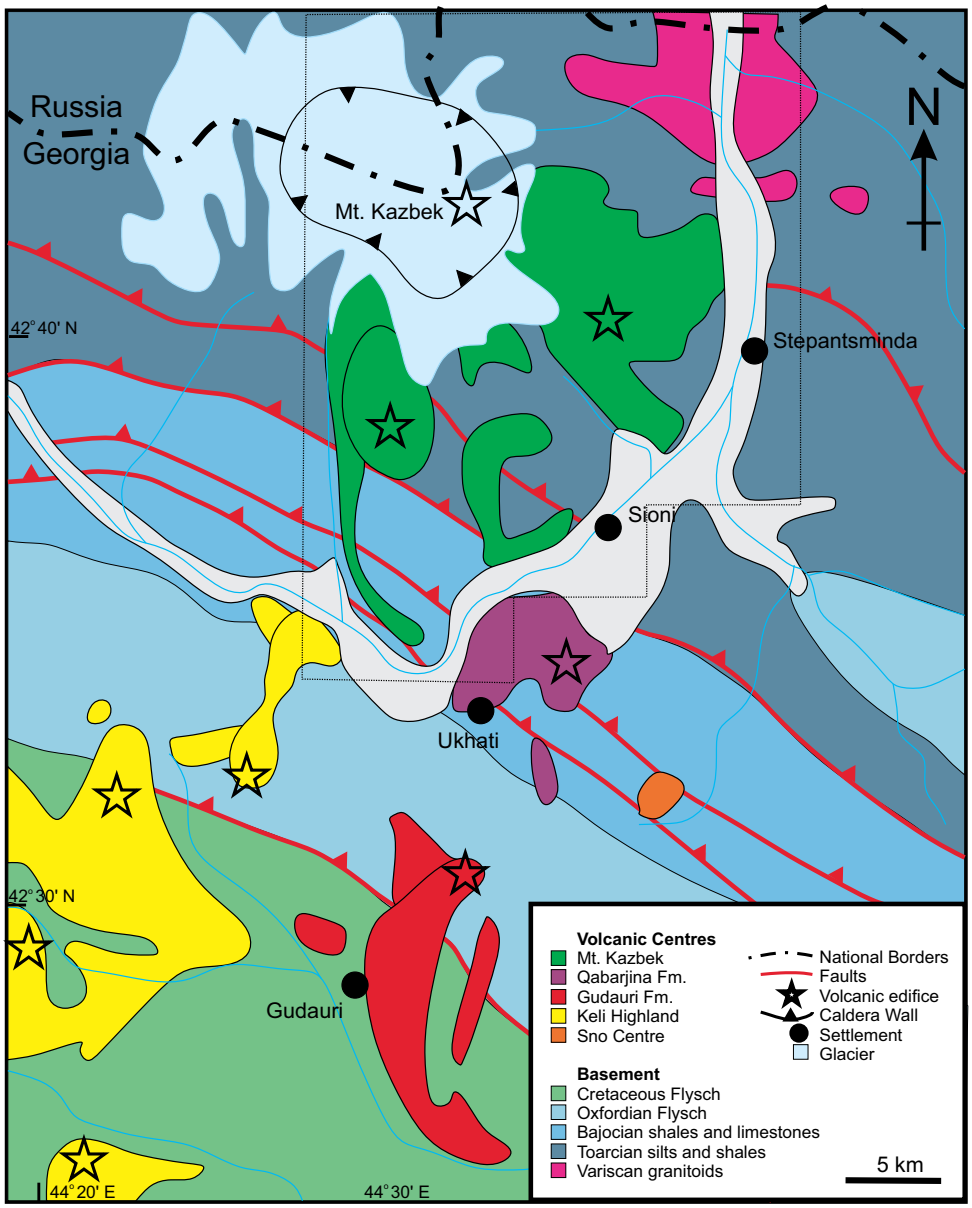

Fig. 2. Simplified geological map of the post-collisional volcanic rocks in the Mt. Kazbek section of the Greater Caucasus and underlying basement rocks. Dotted line shows location of Fig. S1. Adapted by N. Sadradze from Dzotsenidze (1970).

greater than 200 m thick and over 14 km long. Age relationships between the volcanic rocks are shown in Fig. 3.

Mt. Kazbek is the largest stratovolcano in Georgia (altitude, 5054 m). Lebedev *et al.* (2014) distinguished four age groups of volcanic activity. Stage I is older than 400 ka; stage II lasted from 250–200 ka, before a caldera collapse event; stage III was from 120–90 ka; and stage IV occurred at ~50 ka (Fig. 3). This classification is consistent with our morphological observations in the field and therefore we have assigned samples to these four stages. Samples of basement Variscan granitoids were collected to the north of Mt. Kazbek, near the Russian border to assess the composition of potential crustal contaminants (Fig. 3). We also sampled lavas from the Gudauri Formation on east side of the Mthiulethi Aragvi valley, and the Qabarjina Formation around the village of Ukhati. The Keli Highland lies predominantly in the inaccessible territory of South Ossetia, so it was not possible to sample in this area. Detailed field descriptions of the sample locations are presented in the supplementary data.

SAMPLE DESCRIPTIONS

Lavas throughout the Mt. Kazbek region are all porphyritic to varying degrees. Plagioclase and orthopyroxene are almost ubiquitous across all samples with amphibole also a common phenocryst phase. Clinopyroxene, olivine and a sub-calcic high-Al pyroxene (>5 wt % Al_2O_3) occur as a major phenocryst phase in some samples. Olivine is particularly widespread in samples from stage III of the Kazbek volcanics, while apatite and an Fe–Ti oxide are common accessory phases. The

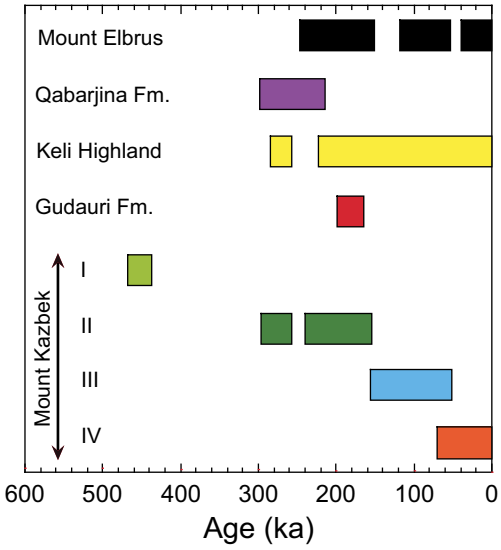

Fig. 3. Compilation of the timings of volcanic activity in the Greater Caucasus. Eruption ages of Mt. Elbrus volcanics are shown as a comparison. Colours correspond to the maps and geochemical figures in the paper. I–IV represent the four stages of volcanic activity identified at Mt. Kazbek. K-Ar ages from Chernyshev *et al.* (2002) and Lebedev *et al.* (2007; 2012).

groundmass is either glassy or dominated by plagioclase, pyroxene and Fe oxides in aphanitic samples. Biotite has only been observed in some stage IV lavas and in trace amounts in the Qabarjina Formation lavas. Mineral proportions and notes on key textural information are provided in Table 1 and typical petrographic features are illustrated in Fig. 4. Detailed information on the field relations and petrology of all volcanic rocks discussed in this study are provided in the supplementary data.

ANALYTICAL TECHNIQUES

Major elements and selected trace element (Sc, V, Cr, Co, Ni, Cu, Zn, Ga, As, S, Rb, Sr, Y, Zr, Nb, Mo, Ba, Pb, Th and U) concentrations were determined by X-ray florescence (XRF). Loss on ignition (LOI) was calculated by measuring the percentage mass loss of volatiles after heating the sample at 1000°C for 40 minutes. Glass disks for major element analyses were made by mixing 0.700 g of the pre-ignited rock powder with dried lithium metaborate–tetraborate flux (Spectraflux 100B) in a ratio of 1:5 by weight and pressed powder pellets were used to determine abundances of trace elements; see Ramsey *et al.* (1995) for details. XRF analysis was undertaken at the Open University using an ARL 8420+ dual goniometer wavelength-dispersive XRF spectrometer following the methodology of Ramsey *et al.* (1995). External reproducibilities of WS-E (Whin Sill dolerite) and OU-3 (Nanhoron microgranite) are better than ±2.5% (2 s.d.) for oxides with a concentration greater than 0.25 wt %. See Thompson *et al.* (2000) for further details of the standards. Trace elements were analysed at the Open University using an Agilent 7500a inductively coupled plasma mass spectrometer (ICP-MS)

Table 1: Mineral modal proportions and textures of samples from the Greater Caucasus

		Plagioclase%	Cpx%	Opx%	High-Al pyx[†]%	Olivine%	Amphibole%	Biotite%	Quartz%	Oxides%	Phenocrysts%	Texture
Kazbegi volcano	Stage 1*	~65	~25	~10	—	—	tr	—	—	tr	60–70	Glassy groundmass
												Trachytic texture
	Stage 2	40–75	<20	3–35	tr	<10	5–25	—	—	<5	30–60	Glassy groundmass
												Vesicular texture (Fig. 4d)
												Plag groups in disequilibrium (Fig. 4d)
	Stage 3	20–30	20–30	10–15	tr	<15	20–30	—	—	tr	15–25	Crystalline groundmass (Fig. 4e)
												Altered amphiboles (Fig. 4e)
	Stage 4	45–60	20–30	5–10	5–10	—	30–50	5–10	tr	—	10–30	Glassy groundmass
												Trachytic texture (Fig. 4f)
Gudauri Fm		15–75	5–15	25–70	5–15	tr	5–10	—	—	—	5–30	Aphanitic groundmass
												Pilotaxytic plag (Fig. 4a)
												Glomerocrysts (Fig. 4b)
Qabarjina Complex		60–80	—	5–15	—	—	15–35	tr	—	tr	30–65	Glassy groundmass
												Fragmented pyroxene (Fig. 4c)
												Glomerocrysts (Fig. 4c)

*Based on single sample. [†]10–16 wt % Al_2O_3.

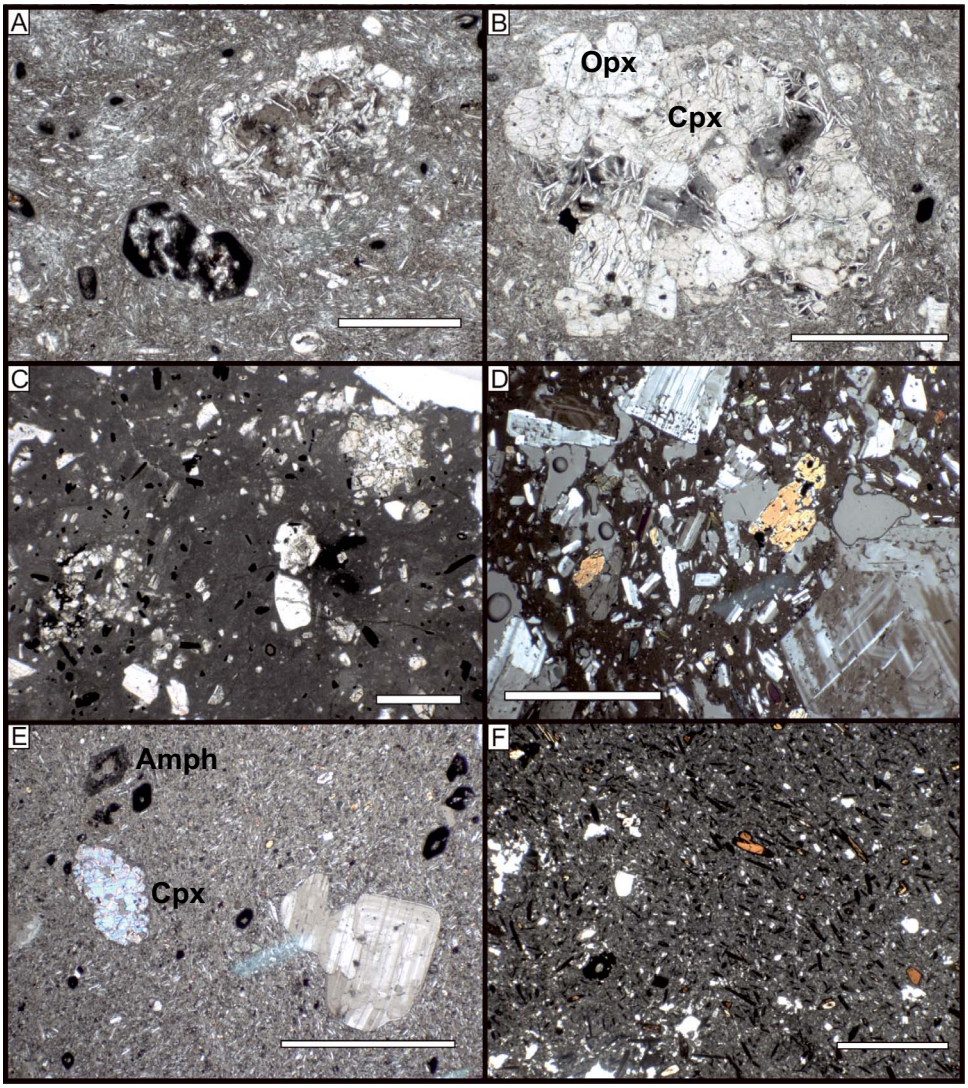

Fig. 4. Textures in representative samples of Quaternary volcanic rocks of the Greater Caucasus. White scale bar is 0.5 mm. (a) Pilotaxytic groundmass in the Gudauri Formation. Two euhedral, but opacitised high-Al pyroxenes. An orthopyroxene-rich glomerocryst is present, with plagioclase laths protruding into trapped melt. (b) Large glomerocryst from the Gudarui Formation, dominated by orthopyroxene (Opx) and clinopyroxene (Cpx), with minor plagioclase, and trapped glass phase. (c) Glassy groundmass of the Qabarjina Formation. The small amphibole phenocrysts are strongly altered, but larger plagioclase phenocrysts are fresh. Pyroxene grains are fragmented, and a pyroxene-dominated glomerocryst is seen in the top right corner. (d) Phenocryst-rich Stage II of Mt. Kazbek volcanics, with two groups of plagioclase grains in disequilibrium. Glassy groundmass, clinopyroxene and vesicles also present. (e) Phenocryst-poor Stage III of Mt. Kazbek volcanics. The groundmass is coarser than other rocks from the area. Amphiboles (Amph) are strongly altered and clinopyroxene (Cpx) is rounded and embayed. (f) Stage IV of Mt. Kazbek volcanics. Phenocrysts are small, and amphibole laths form a trachytic texture.

following the methodology of Rogers *et al.* (2006). Precision was typically <3% (2 s.d.), although Th and U were slightly worse (4.5–6.5%). Comparison between XRF and ICP-MS data is excellent, although for some evolved samples there is an indication of incomplete zircon dissolution. In this study, we present ICP-MS trace element data, because of its better precision and lower detection limits but use XRF Zr data for a small number of evolved samples.

Twenty-four samples were selected for Sr–Pb–Nd isotopic analyses based on major and trace element chemistry, to produce a suite that covers the compositional range. All isotopic measurements were made at the Open University, using a Neptune multi-collector (MC)-ICP-MS. Approximately 0.05 g of sample was leached in 6 M HCl for 1 hour at 120°C, centrifuged for 1 minute, after which the leachate was pipetted off. Samples were then rinsed with MQ H_2O twice and then allowed to dry before being reweighed. The leaching stage is used to remove any potential anthropogenic contaminants. After leaching, the dried powder was digested with concentrated HF-HNO_3, dried and re-dissolved in 6 M HCl and finally dried and re-dissolved in concentrated HNO_3 to produce a complete dissolution. The solution was then split into two aliquots, one for Sr–Pb and the other for Nd isotopic analyses.

Strontium and Pb isotopes were analysed following the methodology developed at the Open University and described in detail by Hunt *et al.* (2012). Instrument reproducibility was monitored by measuring the NBS 987

standard and yields an average $^{87}Sr/^{86}Sr$ of 0.710276 ± 31 (2 s.d., n = 53), although for the early part of the study it yielded 0.710262 ± 6 (2 s.d., n = 26). This change reflects some Faraday cup degradation during the latter part of the study. To correct for the shift, we normalised all our measurements to a preferred MC-ICP-MS value of 0.710266 (Nowell *et al.*, 2003), although the effect on precision is minimal compared to the total variation found in this study.

The rock standards BHVO-2 and AGV-1 were digested and analysed in an identical way to the rock samples to provide a gauge of analytical precision for the whole chemical and mass spectrometric procedure. BHVO-2 yielded an average $^{87}Sr/^{86}Sr$ of 0.703492 ± 11 (2 s.d., n = 4), which is within error of the static TIMS value of 0.703479 ± 20 (Weis *et al.*, 2006), whereas AGV-1 yielded an average of 0.704006 ± 9 (2 s.d., n = 5), which is within error of the static TIMS value of 0.703996 ± 20 (Weis *et al.*, 2006).

Lead isotopes were measured by double-spike by combining an un-spiked run and with a run spiked with a ^{207}Pb–^{204}Pb tracer (see Hunt *et al.*, 2012). Instrument reproducibility was monitored by measuring the NBS 981 standard throughout this study (n = 59 over 30 months) and yields a $^{206}Pb/^{204}Pb$ ratio of 16.9428 ± 24, $^{207}Pb/^{204}Pb$ ratio of 15.5007 ± 28 and a $^{208}Pb/^{204}Pb$ ratio of 36.7276 ± 75, which are within error of previous high-precision double-spike MC-ICP-MS studies (Thirlwall, 2002; Baker *et al.*, 2004; Hunt *et al.*, 2012). AGV-1 was digested 6 times and analysed for Pb isotopes and yielded Pb isotopic values within uncertainty of the high-precision double-spike of Baker *et al.* (2004).

The aliquot for Nd isotopes was first passed through a cation column to separate the rare earth element (REE) from the matrix. Neodymium was then separated from La, Ce and quantitatively from Sm using LnSpec resin in a dilute (0.25 M) HCl media following the method described in Pin *et al.* (2014). Isotopic measurements involved aspirating ~200 ppb via a standard introduction system into the Neptune operating in static low-resolution mode and fitted with H-cones. Analyses were corrected for instrumental mass fractionation using the exponential fractionation law and minor ^{144}Sm interference on ^{144}Nd was stripped off iteratively assuming a $^{146}Nd/^{144}Nd$ ratio of 0.7219 and $^{147}Sm/^{144}Sm$ of 4.83871 (de Laeter *et al.*, 2003; Weis *et al.*, 2006).

Instrument reproducibility was monitored by measuring, a J & M standard that yields an average $^{143}Nd/^{144}Nd$ of 0.511822 ± 25 (2 s.d., n = 58 over 8 months). This standard is tied to a value of the La Jolla standard of 0.511849 ± 3 for $^{143}Nd/^{144}Nd$, which is within error of published data (Raczek *et al.*, 2003; Weis *et al.*, 2006). AGV-1 was digested 6 times and analysed for Nd isotopes and yields an average $^{143}Nd/^{144}Nd$ of 0.512787 ± 15 (2 s.d., n = 6), which is within error of the TIMS values for $^{143}Nd/^{144}Nd$ of 0.512784 ± 18 (Weis *et al.*, 2006).

Major element data for the three centres form strong negative linear trends in plots of MgO, CaO, $Fe_2O_3^{Tot}$ and TiO_2 against SiO_2 with the Gudauri Formation typically forming a cluster at the more mafic end (Fig. 6). The Qabarjina Formation and Stage IV Kazbek volcanics show the most well-defined trends; Stage IV rocks show little variation in MgO, although the MgO content is highest in the most evolved sample.

No overall trend is observed across the whole suite between Al_2O_3 and SiO_2 although the most mafic Gudauri rocks have high- and low-Al_2O_3 groups. Stage III volcanics have a slight positive correlation, while the Qabarjina Formation and Stage IV volcanics define strong negative trends. The Stage IV volcanics have high Al_2O_3 contents, similar to the Gudauri Formation while both sample groups contain high-Al pyroxenes (Table 1). Concentrations of K_2O are relatively constant across the range of SiO_2 (Fig. 5b), particularly for stages II and III of Mt. Kazbek. The Qabarjina Formation shows a positive trend, while Mt. Kazbek Stage IV samples decrease with increasing SiO_2. Na_2O forms a rough positive trend with SiO_2 (Fig. 6g). The Gudauri Formation has lower Na_2O concentrations than the other centres (Na_2O = 3.37–3.79 wt % for Gudauri, 3.83–4.83 wt % for the others). Two parallel trends can be distinguished; a low-Na_2O trend involving the Gudauri Formation, Qabarjina Formation and stage IV volcanics of Mt. Kazbek, and a high-Na_2O one involving the other three stages of Mt. Kazbek. Samples above 59 wt % SiO_2 define a broadly negative trend between SiO_2 and P_2O_5, although the lower SiO_2 Gudauri samples form a positive trend suggesting an inflection point in P_2O_5 at ~59 wt % SiO_2.

RESULTS

Major elements

Geochemical data and sample locations are given in Table 2. All of the samples are fresh, with LOI values between −0.26 and 1.21 wt %, with the highest values corresponding to samples containing hydrous minerals such as amphibole and biotite. Flows from all three centres (Mt. Kazbek, Qabarjina Formation and Gudauri Formation) fall on similar arrays on major-element geochemical plots. All rocks are intermediate to felsic in composition and are classified as sub-alkaline, using the definition of Macdonald & Katsura (1964), although sample 13-056 (Stage III Kazbek lavas) lies close the sub-alkaline to alkaline division (Fig. 5a). The most basic samples are basaltic andesites from the Gudauri flow although two dacitic samples were also sampled from this centre, one at the base of the largest flow, and the second from a separate flow assumed to be associated with the same volcanic centre. Samples from the Qabarjina centre are the most evolved in the region, with compositions that range from andesite to dacite (62.65–67.27 wt % SiO_2). Samples from Mt. Kazbek cover a wide range of compositions from basaltic trachyandesite to dacite (55.83–65.39 wt % SiO_2) consistent with data from Lebedev & Vashakidze (2014). Virtually all samples are quartz normative (Table S1), the exception being sample 13-056

Table 2: Geochemical analyses of samples from the Greater Caucasus; Gudauri Fm

Sample	H1	H2	H3	H4	13-001a	13-002	13-005	13-006
Lat. (° ’N)	42 27.862	42 27.862	42 26.327	42 29.303	42 27.82	42 26.243	42 28.828	42 29.929
Long. (° ’E)	44 28.616	44 28.616	44 29.883	44 28.296	44 28.397	44 29.598	44 28.344	44 27.077
Major elements (wt %)								
SiO_2	57.5	57.1	56.7	57.5	63.0	56.9	57.0	63.8
TiO_2	0.92	0.92	0.95	1.06	0.70	0.98	1.04	0.78
Al_2O_3	16.8	16.6	16.6	18.2	17.8	16.6	18.0	17.1
$Fe_2O_3{}^{TOT}$	6.59	6.59	6.98	6.80	4.44	7.07	6.75	5.02
MnO	0.13	0.13	0.13	0.14	0.09	0.14	0.14	0.11
MgO	5.80	5.88	6.37	4.60	1.94	6.45	4.52	2.33
CaO	6.39	6.32	6.73	6.66	4.51	6.65	6.52	4.04
Na_2O	3.42	3.37	3.38	3.79	4.25	3.39	3.73	4.19
K_2O	1.91	1.89	1.75	1.87	2.29	1.74	1.84	2.28
P_2O_5	0.28	0.27	0.26	0.27	0.30	0.26	0.27	0.24
Total	99.8	99.2	99.9	100.6	99.7	100.2	99.9	99.8
LOI	0.07	0.06	0.03	−0.26	0.40	−0.23	−0.14	0.08
Mg#*	65.96	66.26	66.74	59.82	49.02	66.74	59.58	50.53
Trace elements (ug g^{-1})								
Sc	53.5	55.2	55.8	55.5	9.3	20.4	19.4	12.0
V	128	128	135	138	44.9	20.1	146	77.9
Cr	196	214	235	88.7	45.9	235	87.1	53.1
Co	28.5	27.9	30.4	20.4	10.4	32.2	19.2	-
Ni	123	111	112	33.6	28.3	126	27.2	37.9
Rb	49.1	52.1	46.4	54.0	78.5	48.8	59.3	77.1
Sr	897	947	911	726	687	922	794	437
Y	19.6	21.3	20.6	23.0	16.8	20.8	25.0	17.6
Zr	148	157	146	161	160	148	174	142
Nb	8.43	9.19	8.39	8.66	11.4	7.85	9.60	8.60
Cs	1.96	2.48	1.02	1.67	2.65	0.98	2.10	3.11
Ba	440	459	428	442	503	434	479	453
La	30.0	31.4	28.3	28.1	35.5	28.4	29.3	31.3
Ce	62.2	64.8	58.5	57.7	69.8	59.7	59.9	63.8
Pr	7.27	7.64	6.96	6.75	7.88	6.98	7.07	7.22
Nd	27.2	28.7	26.2	25.5	27.5	26.2	26.0	25.9
Sm	5.02	5.31	4.99	4.99	4.87	5.02	4.98	4.91
Eu	1.42	1.47	1.41	1.44	1.40	1.40	1.50	1.27
Gd	4.15	4.44	4.19	4.46	3.88	4.33	4.49	4.17
Tb	0.61	0.66	0.62	0.68	0.54	0.63	0.68	0.59
Dy	3.35	3.59	3.49	3.86	2.80	3.61	3.86	3.06
Ho	0.67	0.73	0.71	0.79	0.54	0.71	0.79	0.58
Er	1.87	2.05	2.00	2.20	1.54	2.03	2.30	1.55
Yb	1.73	1.90	1.82	2.06	1.31	1.86	2.01	1.27
Lu	0.26	0.28	0.28	0.31	0.20	0.28	0.31	0.19
Hf	3.63	3.73	3.47	3.83	3.80	3.55	4.01	3.44
Pb	14.6	28.1	10.4	16.7	19.1	10.4	10.2	19.7
Th	7.51	7.95	6.71	7.42	9.44	7.14	7.47	9.71
U	1.61	1.73	1.53	1.60	1.80	1.65	1.66	1.51
Isotopic ratios								
$^{87}Sr/^{86}Sr$	0.704183	0.704196	0.704148	0.704435	0.704833	0.704169	0.704444	
2 s.d.	0.000004	0.000004	0.000003	0.000004	0.000005	0.000004	0.000003	
$^{143}Nd/^{144}Nd$	0.512737		0.512734			0.512735	0.512682	
2 s.d.	0.000005		0.000005			0.000009	0.000010	
εNd	1.93		1.86				0.87	
$^{206}Pb/^{204}Pb$	18.590	18.595	18.627	18.598	18.608		18.591	
2 s.d.	0.001	0.001	0.001	0.001	0.001		0.002	
$^{207}Pb/^{204}Pb$	15.614	15.617	15.619	15.616	15.620		15.615	
2 s.d.	0.001	0.001	0.001	0.001	0.001		0.002	
$^{208}Pb/^{204}Pb$	38.653	38.667	38.711	38.660	38.683		38.652	
2 s.d.	0.002	0.003	0.003	0.002	0.002		0.006	

* Mg# assumes Fe^{3+}/Total Fe = 0.1.

(Stage III Kazbek lavas). All follow a calc-alkaline trend on an assimilation and fractional crystallisation (AFC) diagram (not shown). Samples are sodic ($Na_2O/K_2O > 1$), and plot in the low-K, calc-alkaline field in the K_2O v. SiO_2 diagram (Fig. 5b).

Trace elements

Representative trace element variations with SiO_2 are illustrated in Fig. 7, in order to explore any relationships with a measure of melt evolution. Highly incompatible trace elements (e.g. Cs, Rb Th and U) have positive

Table 2: Geochemical analyses of samples from the Greater Caucasus; Qabarjina

Sample	H7	13-045	13-047a	13-049	13-051	13-053	13-055
Lat. (° ’N)	42 33.581	42 34.559	42 34.643	42 34.643	42 34.643	42 34.643	42 35.584
Long. (° ’E)	44 30.742	44 34.481	44 34.123	44 34.123	44 34.123	44 34.123	44 33.298
Major elements (wt %)							
SiO_2	64.6	66.0	62.6	65.9	65.4	67.3	65.1
TiO_2	0.61	0.56	0.71	0.55	0.54	0.49	0.62
Al_2O_3	16.4	16.8	16.9	16.2	16.2	16.3	16.4
Fe_2O_3 ^{TOT}	4.20	3.64	4.47	3.81	3.71	3.00	4.01
MnO	0.10	0.08	0.08	0.09	0.09	0.08	0.10
MgO	2.55	1.48	2.39	1.87	1.80	1.00	2.18
CaO	4.07	3.37	4.27	3.51	3.53	3.23	3.90
Na_2O	4.22	4.48	4.53	4.33	4.33	4.47	4.30
K_2O	2.14	2.52	1.89	2.47	2.41	2.61	2.29
P_2O_5	0.18	0.22	0.24	0.18	0.18	0.15	0.21
Total	99.1	99.3	98.1	98.9	98.2	98.6	99.1
LOI	0.17	0.15	0.94	0.66	1.21	0.51	0.64
Mg#*	57.19	47.20	54.07	51.94	51.65	42.30	54.43
Trace elements (ug g^{-1})							
Sc	32.3	8.52	10.7	8.33	9.03	7.10	9.42
V	72.5	43.6	83.0	55.7	58.9	26.5	62.9
Cr	85.4	40.3	43.3	46.2	44.2	11.6	52.2
Co	13.4	9.27	12.3	9.08	8.40	4.61	8.85
Ni	28.6	18.7	22.7	19.4	12.1	7.2	16.0
Rb	72.8	93.1	67.2	84.6	91.4	88.1	72.0
Sr	464	395	540	432	469	411	440
Y	15.7	15.0	16.6	15.5	16.2	15.9	15.2
Zr	164	43.4	116	112	120	195	154
Nb	8.67	9.62	25.0	8.66	9.41	8.47	7.88
Cs	5.27	4.53	4.41	6.66	7.07	6.52	5.45
Ba	401	489	592	471	484	474	422
La	28.6	32.7	34.5	30.8	32.8	32.4	29.0
Ce	56.0	65.5	67.1	59.6	63.7	62.2	56.9
Pr	6.10	7.04	7.77	6.42	6.75	6.69	6.19
Nd	21.7	25.0	27.6	21.8	23.5	22.6	21.3
Sm	4.07	4.59	5.09	3.96	4.30	4.05	3.95
Eu	1.04	1.07	1.33	1.02	1.06	1.00	1.03
Gd	3.37	3.71	3.95	3.27	3.51	3.35	3.29
Tb	0.49	0.53	0.56	0.47	0.51	0.48	0.48
Dy	2.62	2.80	2.92	2.54	2.82	2.62	2.58
Ho	0.52	0.51	0.56	0.50	0.53	0.51	0.51
Er	1.45	1.35	1.50	1.43	1.49	1.51	1.47
Yb	1.35	1.16	1.29	1.25	1.38	1.36	1.30
Lu	0.20	0.16	0.19	0.19	0.20	0.21	0.20
Hf	3.82	1.45	3.22	2.94	3.11	4.73	3.91
Pb	18.9	23.6	20.7	21.7	24.7	21.4	20.3
Th	10.0	10.2	12.9	11.9	12.9	11.7	10.6
U	2.41	1.84	2.69	2.86	3.22	2.92	2.65
Isotopic ratios							
$^{87}Sr/^{86}Sr$	0.704869			0.704947			
2 s.d.	0.000003			0.000005			
$^{143}Nd/^{144}Nd$	0.512690			0.512659			0.512663
2 s.d.	0.000006			0.000009			0.000009
εNd	1.02			0.41			0.48
$^{206}Pb/^{204}Pb$	18.627			18.618			18.588
2 s.d.	0.001			0.001			0.002
$^{207}Pb/^{204}Pb$	15.619			15.618			15.600
2 s.d.	0.001			0.001			0.002
$^{208}Pb/^{204}Pb$	38.693			38.688			38.621
2 s.d.	0.003			0.003			0.005

* Mg# assumes Fe^{3+}/Total Fe = 0.1.

correlations with SiO_2 although La, Ba and Nb do not show such systematic relationships. Moderately incompatible trace elements such as Zr, Hf and Sm do not define any strong correlations with SiO_2 or any other indicator of melt evolution such as Mg#. Moderately compatible elements such as Cr, V and Sr define good negative correlations with SiO_2. In detail, the Gudauri Formation typically shows the highest concentrations (up to 235 μg g^{-1} Cr), with the Kazbek flows having intermediate values (28–188 μg g^{-1} Cr), and the Qabarjina

Table 2: Geochemical analyses of samples from the Greater Caucasus; Kazbek Stage I

Sample	13-008
Lat. (° 'N)	42 35.051
Long. (° 'E)	44 28.440
Major elements (wt %)	
SiO_2	62.8
TiO_2	0.74
Al_2O_3	16.3
Fe_2O_3 TOT	4.61
MnO	0.08
MgO	3.48
CaO	5.03
Na_2O	4.83
K_2O	1.62
P_2O_5	0.21
Total	99.6
LOI	0.07
Mg#*	62.42
Trace elements (ug g^{-1})	
Sc	11.1
V	75.0
Cr	103
Co	17.2
Ni	43.7
Rb	45.3
Sr	464
Y	12.4
Zr	98.0
Nb	6.00
Cs	1.11
Ba	412
La	23.5
Ce	45.6
Pr	5.12
Nd	18.2
Sm	3.48
Eu	1.07
Gd	3.03
Tb	0.43
Dy	2.36
Ho	0.46
Er	1.29
Yb	1.10
Lu	0.16
Hf	2.87
Pb	14.4
Th	8.77
U	2.24
Isotopic ratios	
$^{87}Sr/^{86}Sr$	
2 s.d.	
$^{143}Nd/^{144}Nd$	
2 s.d.	
εNd	
$^{206}Pb/^{204}Pb$	
2 s.d.	
$^{207}Pb/^{204}Pb$	
2 s.d.	
$^{208}Pb/^{204}Pb$	
2 s.d.	

* Mg# assumes Fe^{3+}/Total Fe = 0.1.

Formation the lowest (85.4–11.6 μg g^{-1} Cr). Two samples from the Gudauri Formation (H4 and 13-005) have anomalously low Cr, which also show low Al_2O_3 contents, suggesting a mineralogical control on the distribution of these elements. In common with the major elements, there is an indication that the Gudauri Formation and stage IV Kazbek samples define distinct trends relative to the other lava groups, with these two groups also having elevated concentrations of Sr and the heavy REE (HREE) element Yb (and Y).

Primitive-mantle normalised variation plots for all three centres show similar patterns (Fig. 8) with large ion lithophile elements (LILEs) enrichment relative to high field strength elements (HFSEs), large negative Nb anomalies and positive Pb anomalies. Enrichment in LILEs is typically in the order of 55–153 (for Rb and Ba), relative to primitive mantle. The greatest enrichment occurs in the Qabarjina Formation, reflecting the broad positive trend of Rb with SiO_2. The Gudauri Formation typically shows a smaller negative Nb anomaly (Nb/Nb* >0.2) than the Qabarjina Formation (0.135–0.201) and Mt. Kazbek centres (0.135–0.297), where Nb/Nb* is the ratio between the primitive-mantle normalised Nb abundance and the interpolated value between primitive-mantle normalised U and K abundances (Fig. 8). We also illustrate trace element data for a representative Hercynian granite that is part of the basement through which the Mt. Kazbek magmas traversed (Fig. 8f). The granite has a trace element pattern broadly similar to the Mt. Kazbek region magmas, but has significantly less enrichment in Rb and Cs, is significantly depleted in Sr and has relatively more enrichment in Th and K.

Chondrite-normalised plots of REEs (Fig. 9) have similar patterns between all three centres. The majority of samples lacks a significant Eu-anomaly (Eu/Eu* = 0.79–1.03, although most are >0.9; Eu anomaly is defined as $Eu_N/(Sm_N \times Gd_N)0^{.5}$, where each of the elements is chondrite normalised). Light REE (LREEs) are enriched relative to HREEs in all samples, with variation in the HREE greater than in the LREE, which controls the degree of LREE enrichment as defined by $[La/Yb]_N$. Stage IV lavas from Mt. Kazbek together with those from the Gudauri centre had the smallest LREE enrichment ($[La/Yb]_N$ = 9.25–13.60), whereas Stages II and III have the steepest REE patterns, and the Qabarjina Formation samples plot at intermediate values. The slope of the MREE to HREEs was monitored by $[Dy/Yb]_N$ as this ratio is sensitive to both residual garnet in the mantle source and amphibole fractionation. Stages II and III of Mt. Kazbek again have the highest $[Dy/Yb]_N$ (1.35–1.65). The Gudauri and Qabarjina formations and Stage IV of Mt. Kazbek have relatively flat patterns ($[Dy/Yb]_N$ = 1.23–1.33). The Hercynian granite has a LREE enrichment similar to the least enriched lava ($[La/Yb]_N$ = 10.7), a relatively flat MREE to HREEs slope ($[Dy/Yb]_N$ = 1.26) and a significant negative Eu anomaly of 0.62.

Isotopes

Twenty-four samples were analysed for Sr- and Pb-isotopic composition with 14 of these samples analysed for Nd isotopes. No age correction has been undertaken because all samples are <450 ka (Lebedev *et al.*, 2008) and the correction is smaller than the analytical uncertainty. Variations in composition are small, but $^{87}Sr/^{86}Sr$ and $^{143}Nd/^{144}Nd$ form a negative correlation that sits well within the mantle array (Fig. 10). The Gudauri and Mt.

Table 2: Geochemical analyses of samples from the Greater Caucasus; Kazbek Stage II

Sample	13-026	13-028	13-030	13-032	13-034	13-035	13-037
Lat. (° ’N)	42 40.001	42 40.036	42 40.114	42 40.068	42 34.568	42 41.584	42 41.303
Long. (° ’E)	44 38.297	44 38.372	44 38.254	44 38.277	44 34.477	44 38.151	44 38.139
Major elements (wt %)							
SiO_2	62.2	63.4	62.0	62.2	62.3	59.5	59.2
TiO_2	0.77	0.77	0.77	0.80	0.80	1.01	1.05
Al_2O_3	16.0	16.4	16.0	16.5	16.5	16.6	16.6
Fe_2O_3 ^{TOT}	4.85	4.77	4.75	5.03	4.99	6.13	6.11
MnO	0.08	0.08	0.08	0.09	0.09	0.10	0.09
MgO	3.93	3.78	3.66	3.05	3.04	4.62	4.09
CaO	5.28	5.10	5.00	4.96	4.99	5.70	5.49
Na_2O	4.74	4.80	4.59	4.59	4.65	4.65	4.62
K_2O	1.68	1.88	1.90	1.93	1.92	1.83	1.84
P_2O_5	0.24	0.30	0.27	0.28	0.28	0.35	0.36
Total	99.7	101.2	99.0	99.5	99.5	100.5	99.5
LOI	−0.07	0.08	0.07	0.01	0.38	0.22	0.20
Mg#*	64.07	63.56	62.92	57.17	57.29	62.43	59.53
Trace elements (ug g^{-1})							
Sc	12.4	11.5	11.4	13.1	12.5	13.5	12.6
V	131	103	85.2	104	85.7	100	115
Cr	115	111	116	66.3	75.5	158	118
Co	18.3	16.8	17.6	16.6	15.6	21.1	20.9
Ni	86.8	55.2	55.7	32.0	60.6	30.4	53.6
Rb	46.3	53.2	59.7	59.4	52.5	45.9	51.5
Sr	522	574	600	610	582	608	653
Y	13.0	12.3	13.5	13.5	12.6	15.1	17.1
Zr	135	125	119	155	153	166	187
Nb	6.41	7.02	8.92	10.7	7.81	9.02	11.7
Cs	1.32	3.15	2.04	2.91	3.52	2.77	3.62
Ba	415	491	513	459	445	506	510
La	26.2	28.9	29.9	29.1	28.4	30.6	31.8
Ce	50.0	54.6	57.1	56.4	54.1	60.2	62.7
Pr	5.66	6.07	6.47	6.23	6.06	6.92	7.36
Nd	20.0	21.2	22.8	22.4	21.3	24.8	26.6
Sm	3.67	3.84	4.18	4.18	3.92	4.66	5.23
Eu	1.13	1.17	1.17	1.18	1.16	1.38	1.41
Gd	3.16	3.14	3.29	3.44	3.25	3.92	4.14
Tb	0.45	0.43	0.46	0.48	0.44	0.54	0.59
Dy	2.32	2.22	2.37	2.48	2.32	2.79	3.05
Ho	0.45	0.43	0.45	0.47	0.44	0.53	0.57
Er	1.26	1.19	1.19	1.23	1.21	1.42	1.47
Yb	1.07	0.96	1.02	1.07	1.02	1.17	1.24
Lu	0.16	0.15	0.15	0.16	0.15	0.17	0.18
Hf	3.43	3.17	2.95	3.70	3.87	4.10	4.30
Pb	12.4	15.4	14.0	14.0	13.5	15.0	15.1
Th	9.23	9.46	10.4	8.81	8.64	9.68	10.6
U	2.30	2.52	2.62	2.27	2.29	2.32	2.44
Isotopic ratios							
$^{87}Sr/^{86}Sr$	0.704430	0.704477				0.704561	
2 s.d.	0.000005	0.000005				0.000005	
$^{143}Nd/^{144}Nd$						0.512743	
2 s.d.						0.000015	
εNd						2.05	
$^{206}Pb/^{204}Pb$	18.647	18.646				18.646	
2 s.d.	0.001	0.001				0.003	
$^{207}Pb/^{204}Pb$	15.617	15.623				15.626	
2 s.d.	0.001	0.001				0.002	
$^{208}Pb/^{204}Pb$	38.739	38.746				38.742	
2 s.d.	0.002	0.003				0.007	

* Mg# assumes Fe^{3+}/Total Fe = 0.1.

Kazbek samples have overlapping $^{87}Sr/^{86}Sr$ (0.70415–0.70456). For a given $^{87}Sr/^{86}Sr$, the Gudauri Formation has lower $^{143}Nd/^{144}Nd$ (Mt. Kazbek, 0.51274–0.51280, εNd = 0.48–3.18; Gudauri Formation, 0.51268–0.51274, εNd = 0.87–1.93). The Qabarjina Formation plots with more radiogenic Sr ($^{87}Sr/^{86}Sr$ = 0.70487–0.70495) and lower Nd ($^{143}Nd/^{144}Nd$ = 0.51266–0.51269, εNd = 0.41–1.02) isotopes. Within the Mt. Kazbek samples, Stage II is more radiogenic than Stage III, while Stage IV shows a displacement to lower $^{143}Nd/^{144}Nd$, comparable to that

Table 2: Geochemical analyses of samples from the Greater Caucasus; Kazbek Stage II

Sample	13-038	13-040	13-043	13-059	13-062	13-067
Lat. (° ’N)	42 41.665	42 40.266	42 40.266	42 37.859	42 37.705	42 37.253
Long. (° ’E)	44 38.501	44 37.842	44 37.842	44 36.759	44 36.245	44 35.523
Major elements (wt %)						
SiO_2	61.9	58.6	61.9	63.2	61.8	62.0
TiO_2	0.77	0.98	0.80	0.64	0.73	0.77
Al_2O_3	15.9	16.4	16.4	15.8	16.6	16.4
Fe_2O_3 ^{TOT}	4.76	5.95	5.02	4.14	4.97	5.09
MnO	0.08	0.10	0.09	0.07	0.10	0.10
MgO	3.64	4.31	3.07	2.87	3.43	3.40
CaO	4.86	5.56	4.94	4.62	4.76	4.55
Na_2O	4.66	4.46	4.57	4.72	4.27	4.36
K_2O	1.93	1.82	1.93	1.79	2.04	2.11
P_2O_5	0.30	0.34	0.29	0.21	0.26	0.28
Total	98.8	98.5	99.0	98.0	99.0	99.1
LOI	0.44	0.56	0.61	1.18	−0.12	−0.07
Mg#*	62.76	61.44	57.38	60.46	60.28	59.49
Trace elements (ug g^{-1})						
Sc	11.4	13.5	12.9	10.6	13.2	12.9
V	114	109	86.3	99.5	94.8	92.4
Cr	106	163	67.0	72.2	102	107
Co	16.8	22.3	15.5	14.4	16.3	15.2
Ni	74.8	69.3	60.9	29.7	49.3	44.6
Rb	55.2	51.6	54.0	52.2	62.9	68.0
Sr	562	654	584	511	527	555
Y	12.8	16.4	12.8	11.4	15.9	16.5
Zr	120	180	158	141	130	146
Nb	7.47	11.2	7.96	6.04	8.56	14.8
Cs	3.59	3.12	4.39	3.37	2.37	2.61
Ba	483	506	443	386	425	449
La	29.9	32.2	28.5	23.7	30.2	32.1
Ce	57.1	63.3	54.2	45.6	60.1	63.8
Pr	6.39	7.39	6.02	5.01	6.71	7.14
Nd	22.3	26.7	21.2	17.6	23.8	25.2
Sm	4.01	5.12	3.91	3.19	4.45	4.70
Eu	1.18	1.41	1.16	1.00	1.23	1.27
Gd	3.33	4.09	3.18	2.77	3.72	3.91
Tb	0.46	0.58	0.44	0.39	0.53	0.54
Dy	2.33	2.98	2.28	2.02	2.80	2.88
Ho	0.44	0.55	0.44	0.39	0.55	0.55
Er	1.21	1.44	1.20	1.09	1.56	1.53
Yb	1.01	1.21	1.01	0.93	1.32	1.32
Lu	0.15	0.18	0.15	0.14	0.20	0.19
Hf	3.09	4.12	3.79	3.48	3.39	3.93
Pb	14.6	15.1	13.2	18.7	17.0	16.7
Th	9.39	10.0	8.38	8.11	8.88	9.42
U	2.53	2.27	2.21	2.28	2.09	2.29
Isotopic ratios						
$^{87}Sr/^{86}Sr$	0.704475		0.704557	0.704341		
2 s.d.	0.000004		0.000004	0.000004		
$^{143}Nd/^{144}Nd$				0.512770		
2 s.d.				0.000011		
εNd				2.57		
$^{206}Pb/^{204}Pb$	18.644		18.641	18.634		
2 s.d.	0.001		0.001	0.001		
$^{207}Pb/^{204}Pb$	15.624		15.622	15.622		
2 s.d.	0.001		0.001	0.001		
$^{208}Pb/^{204}Pb$	38.747		38.738	38.745		
2 s.d.	0.003		0.003	0.003		

* Mg# assumes Fe^{3+}/Total Fe = 0.1.

of the Gudarui Formation. The Greater Caucasus samples overlap slightly with Lesser Caucasus samples (Neill *et al.*, 2013, 2015; Sugden *et al.*, 2019) but extend to less radiogenic Nd isotope values.

Lead isotopes also show small variations (Fig. 11). Positive trends are formed between $^{206}Pb/^{204}Pb$ and $^{207}Pb/^{204}Pb$ or $^{208}Pb/^{204}Pb$, which are resolvable because of the high-precision double spike measurements. Similarly to Sr and Nd isotopes, the Gudauri Formation forms the least radiogenic part of the trend ($^{206}Pb/^{204}Pb$ = 18.59–18.61). Mt. Kazbek extends to the most radiogenic values ($^{206}Pb/^{204}Pb$ = 18.59–18.67), while the Qabarjina

Table 2: Geochemical analyses of samples from the Greater Caucasus; Kazbek Stage III

Sample	13-025	13-056	13-070	13-071	13-072	13-073
Lat. (° ’N)	42 40.019	42 39.556	42 40.273	42 40.273	Float	Float
Long. (° ’E)	44 37.799	44 34.576	44 37.235	44 37.235	Float	Float
Major elements (wt %)						
SiO_2	59.0	55.8	59.5	58.6	60.1	59.9
TiO_2	1.03	1.30	1.05	1.03	0.85	0.85
Al_2O_3	15.8	16.3	15.8	15.7	16.2	16.1
Fe_2O_3 ^{TOT}	6.04	7.63	6.14	6.01	5.30	5.35
MnO	0.09	0.12	0.09	0.09	0.08	0.08
MgO	4.93	5.93	5.06	4.90	4.70	4.75
CaO	5.88	6.46	5.95	5.79	5.73	5.77
Na_2O	4.51	4.54	4.53	4.40	4.48	4.53
K_2O	1.78	1.65	1.79	1.76	1.69	1.70
P_2O_5	0.32	0.40	0.33	0.31	0.32	0.32
Total	99.5	100.1	100.3	98.6	99.4	99.4
LOI	−0.08	−0.24	−0.12	−0.16	−0.07	0.11
Mg#∗	64.22	63.14	64.47	64.22	66.10	66.15
Trace elements (ug g^{-1})						
Sc	16.1	15.8	16.7	16.0	13.4	14.5
V	107	138	131	138	105	118.9
Cr	158	188	148	167	158	154
Co	21.1	32.0	23.0	23.5	21.0	21.0
Ni	16.3	93.2	84.0	86.5	93.5	96.8
Rb	43.5	39.4	42.0	46.7	48.3	45.3
Sr	670	681	665	699	646	625
Y	12.7	18.7	12.7	13.7	13.3	12.9
Zr	92.2	197	124	131	174	173
Nb	7.92	12.7	8.0	9.6	8.9	9.4
Cs	2.42	0.95	1.6	2.0	2.2	3.0
Ba	403	546	399	414	421	410
La	26.7	29.1	25.9	27.5	27.8	27.3
Ce	51.6	58.3	51.2	53.8	53.9	52.7
Pr	5.88	6.97	5.85	6.25	6.17	5.96
Nd	20.9	25.9	21.1	22.6	22.0	21.1
Sm	3.89	5.25	3.90	4.30	4.16	3.84
Eu	1.21	1.56	1.24	1.24	1.19	1.19
Gd	3.28	4.42	3.37	3.45	3.27	3.22
Tb	0.44	0.65	0.46	0.48	0.46	0.46
Dy	2.27	3.39	2.39	2.47	2.40	2.30
Ho	0.43	0.64	0.45	0.47	0.45	0.44
Er	1.16	1.65	1.23	1.23	1.18	1.21
Yb	0.90	1.37	0.98	1.01	1.03	1.02
Lu	0.14	0.19	0.15	0.15	0.15	0.15
Hf	2.54	4.48	3.10	3.19	4.19	4.21
Pb	9.5	13.6	8.8	10.0	14.4	11.6
Th	6.09	8.92	7.10	8.11	9.38	8.47
U	1.33	2.16	1.98	2.15	2.38	2.34
Isotopic ratios						
$^{87}Sr/^{86}Sr$	0.704318	0.704214	0.704305			0.704407
2 s.d.	0.000005	0.000003	0.000003			0.000006
$^{143}Nd/^{144}Nd$		0.512801	0.512770			0.512783
2 s.d.		0.000007	0.000007			0.000011
εNd						2.83
$^{206}Pb/^{204}Pb$	18.648	18.675	18.623			18.636
2 s.d.	0.002	0.001	0.001			0.001
$^{207}Pb/^{204}Pb$	15.625	15.623	15.619			15.619
2 s.d.	0.002	0.001	0.001			0.001
$^{208}Pb/^{204}Pb$	38.755	38.764	38.705			38.727
2 s.d.	0.005	0.002	0.004			0.003

∗ Mg# assumes Fe^{3+}/Total Fe = 0.1.

Formation plots at intermediate values ($^{206}Pb/^{204}Pb$ = 18.59–18.63). $^{207}Pb/^{204}Pb$ has a very restricted composition ($^{207}Pb/^{204}Pb$ = 15.614–15.626), while $^{208}Pb/^{204}Pb$ ranges from 38.65–38.76. The trends run sub-parallel to the northern hemisphere reference line (NHRL, Hart, 1984), with all samples lying above the NHRL, although a single sample from the Qabajina Formation plots off the trend closer to the NHRL. In detail, the Gudauri and Kazbek Group IV lavas plot as a resolvable group at a lower $^{206}Pb/^{204}Pb$ for a given $^{207}Pb/^{204}Pb$ (Fig. 11b). The Mt. Kazbek samples plot close to contemporaneous volcanic rocks in the Lesser Caucasus (Neill *et al.*, 2013, 2015)

Table 2: Geochemical analyses of samples from the Greater Caucasus; Kazbek Stage IV

Sample	H5	H6	KZ1	13-012
Lat. (° ’N)	42 36.277	42 36.344	42 36.243	42 34.571
Long. (° ’E)	44 34.457	44 34.484	44 34.486	44 34.476
Major elements (wt %)				
SiO_2	64.0	59.6	61.3	62.0
TiO_2	0.67	0.79	0.72	0.71
Al_2O_3	16.3	17.9	17.3	17.1
Fe_2O_3 ^{TOT}	4.47	5.66	5.16	5.05
MnO	0.08	0.12	0.11	0.11
MgO	3.41	2.96	2.93	2.96
CaO	4.76	5.87	5.48	5.33
Na_2O	4.47	3.83	3.97	4.03
K_2O	1.89	2.40	2.39	2.36
P_2O_5	0.23	0.29	0.26	0.26
Total	100.2	99.4	99.6	99.9
LOI	0.05	0.11	0.00	0.13
Mg#*	62.70	53.52	55.59	56.35
Trace elements (ug g^{-1})				
Sc	35.0	39.2	39.7	12.1
V	82.7	116	105	79.7
Cr	112	27.7	52.2	65.6
Co	16.4	13.8	13.6	12.4
Ni	61.4	8.9	13.5	37.2
Rb	56.1	75.3	76.3	70.2
Sr	529	928	809	719
Y	13.5	20.6	18.9	16.5
Zr	107	158	135	119
Nb	7.47	8.89	8.53	7.04
Cs	3.88	4.94	5.38	5.22
Ba	387	655	612	589
La	27.8	34.9	32.9	30.6
Ce	53.6	70.1	66.1	60.9
Pr	5.89	8.00	7.33	6.89
Nd	20.9	28.9	26.3	24.1
Sm	3.86	5.15	4.72	4.31
Eu	1.03	1.42	1.28	1.22
Gd	3.17	4.26	3.88	3.61
Tb	0.45	0.62	0.57	0.53
Dy	2.37	3.37	3.14	2.91
Ho	0.46	0.68	0.64	0.59
Er	1.24	1.92	1.77	1.71
Yb	1.10	1.80	1.65	1.52
Lu	0.16	0.27	0.25	0.24
Hf	2.65	3.78	3.37	3.31
Pb	15.9	18.5	19.9	20.2
Th	8.42	10.2	10.3	10.1
U	1.95	2.27	2.39	2.47
Isotopic ratios				
$^{87}Sr/^{86}Sr$	0.704505	0.704360	0.704339	0.704363
2 s.d.	0.000004	0.000004	0.000004	0.000004
$^{143}Nd/^{144}Nd$		0.512738		0.512756
2 s.d.		0.000004		0.000012
εNd		1.96		2.30
$^{206}Pb/^{204}Pb$	18.592	18.600	18.604	18.606
2 s.d.	0.001	0.001	0.001	0.001
$^{207}Pb/^{204}Pb$	15.617	15.617	15.615	15.620
2 s.d.	0.001	0.001	0.001	0.001
$^{208}Pb/^{204}Pb$	38.665	38.662	38.666	38.682
2 s.d.	0.002	0.002	0.002	0.002

* Mg# assumes Fe^{3+}/Total Fe = 0.1.

but have consistently lower $^{206}Pb/^{204}Pb$, ratios, while they have similar $^{206}Pb/^{204}Pb$ ratios than lavas from Mt. Elbrus but with distinctly lower $^{208}Pb/^{204}Pb$ ratios and particularly $^{207}Pb/^{204}Pb$ ratios (Lebedev *et al.*, 2010; Chugaev *et al.*, 2013).

DISCUSSION

Fractional crystallisation

The most primitive compositions (from the Gudauri Formation) are SiO_2-rich basaltic andesites, with Mg# ~65. All other centres have MgO <5 wt %. None of the lavas

Table 2: Geochemical analyses of samples from the Greater Caucasus; Variscan Granites

Sample	13-020	13-021	13-022
Lat. (° ’N)	42 42.620	42 42.620	42 42.620
Long. (° ’E)	44 37.638	44 37.638	44 37.638
Major elements (wt %)			
SiO_2	—	65.9	—
TiO_2	—	0.61	—
Al_2O_3	—	15.7	—
Fe_2O_3	—	5.14	—
MnO	—	0.10	—
MgO	—	1.77	—
CaO	—	4.45	—
Na_2O	—	3.22	—
K_2O	—	2.83	—
P_2O_5	—	0.19	—
Total	—	99.9	—
LOI	—	1.12	—
Mg#	—	—	—
Trace elements (ppm)			
Sc	14.8	12.8	7.2
V	95.7	95.1	—
Cr	28.9	49.7	24.2
Co	—	—	—
Ni	7.9	7.1	7.5
Rb	64.1	82.2	100.0
Sr	226	200	236
Y	27.4	24.0	16.4
Zr	161	152	150
Nb	10.1	8.7	7.7
Cs	1.73	2.33	2.71
Ba	152	502	603
La	36.3	33.5	35.3
Ce	72.0	66.4	67.0
Pr	8.04	7.39	7.06
Nd	29.0	26.4	23.5
Sm	5.79	5.26	3.99
Eu	1.05	1.01	1.09
Gd	5.22	4.63	3.20
Tb	0.81	0.72	0.48
Dy	4.70	4.15	2.67
Ho	0.94	0.82	0.53
Er	2.64	2.33	1.55
Yb	2.45	2.17	1.50
Lu	0.35	0.32	0.22
Hf	0.14	0.22	0.11
Pb	12.6	16.6	21.1
Th	14.6	13.3	15.2
U	2.71	1.83	2.53
Isotopic ratios			
$^{87}Sr/^{86}Sr$	—	0.711836	—
2 s.d.	—	0.000006	—
$^{143}Nd/^{144}Nd$	—	0.512186	—
2 s.d.	—	0.000012	
εNd	—	−8.82	—
$^{206}Pb/^{204}Pb$	20.020	19.420	18.935
2 s.d.	0.002	0.001	0.001
$^{207}Pb/^{204}Pb$	15.757	16.316	15.71
2 s.d.	0.002	0.001	0.001
$^{208}Pb/^{204}Pb$	41.371	41.594	39.552
2 s.d.	0.006	0.004	0.004

has Mg# or Ni contents that are high enough to be in equilibrium with mantle olivine and therefore no lava we collected from the Mt. Kazbek region represents a primary magma from a peridotitic mantle source. However, the presence of minor olivine and clinopyroxene, both with Mg-rich cores, make it a reasonable assumption that all lavas from the Greater Caucasus have previously undergone significant fractionation of olivine, pyroxene and Cr-spinel.

The presence of complex zoning in plagioclase, amphibole and clinopyroxene and of disequilibrium features such as embayed pyroxenes, reaction rims,

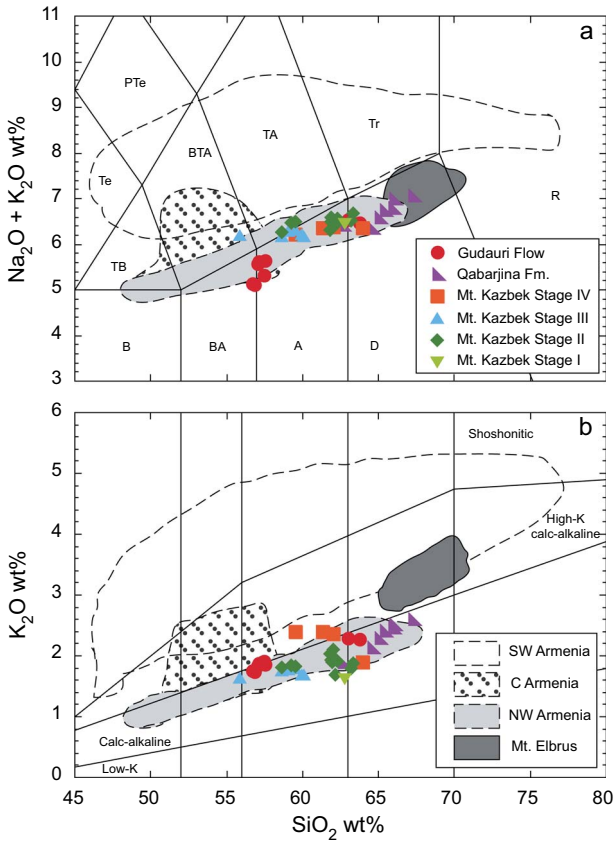

Fig. 5. Chemical classification of the lavas from the Greater Caucasus volcanics analysed in this study. (a) Total alkalis versus SiO_2 classification diagram (after Le Bas *et al.*, 1986). Also illustrated are fields for compositions from recent volcanics from the Lesser Caucasus in Armenia. For simplicity these have been subdivided into three distinct areas; SW Armenia (Vardenis and Syunik volcanic fields; Sugden *et al.*, 2019), central Armenia (Yerevan volcanic field; Neill *et al.*, 2015) and NW Armenia (Shirak and Lori volcanic fields; Neill *et al.*, 2013, 2015). The field for Mt. Elbrus in the Greater Caucasus uses data from Gurbanov *et al.* (2004) and Lebedev *et al.* (2010). Abbreviations for the fields are B, basalt; BA, basaltic andesite; A, andesite; D, dacite; R, rhyolite; TB, trachybasalt; BTA, basaltic trachyandesite; TA, trachyandesite; Tr, trachyte; Te, tephrite/basanite; PTe, phonotephrite. (b) K_2O versus SiO_2 classification diagram (modified from Peccerillo & Taylor, 1976) for the same datasets, with fields for low-K, low-K calc-alkaline, high-K calc-alkaline and shoshinitic. In both plots 2 se uncertainties are smaller than the symbol size.

sieved plagioclase and rounding of grains is indicative that samples may record multiple pulses of magmatism and mixing of melts. Furthermore, the phenocryst-rich nature of some of the lavas may obscure some of the fractionation trends, such as the variation in Al_2O_3 and Cr at constant SiO_2 observed in the Gudauri Formation. However, some clear conclusions can be made on the fractionation history. Overall, there are strong negative correlations between CaO, $Fe_2O_3^{Tot}$, MgO, MnO and TiO_2 with SiO_2. These trends are consistent with fractionation of the observed mineral assemblage (plagioclase, orthopyroxene, clinopyroxene, amphibole and Fe–Ti oxide) in approximately the proportions found in the phenocryst assemblages. There is a limited range in Al_2O_3 concentrations, with no distinct overall trend, apart from in Stage IV of Mt. Kazbek and the Qabarjina Formation, where there are good negative correlations. These observations require plagioclase to be a crystallising phase over the whole range of SiO_2 as the crystal extract has to have enough Al_2O_3 to keep the Al_2O_3 relatively constant for most lava groups. Additionally, samples from the Qabarjina Formation and from the youngest (Stage IV) Kazbek lavas have (1) larger negative Eu anomalies (Eu/Eu* = 0.79–0.90) and (2) strong negative correlations between Al_2O_3 and Sr with SiO_2, which together suggest that the proportion of plagioclase crystallising increases at high SiO_2 and in the youngest magmas. Potassium shows very little variation with SiO_2, indicating it may be buffered by a potassic phase such as amphibole consistent with petrographic observations. By contrast, Mt. Kazbek Stage IV lavas have an inflection in K_2O at ~62 wt % SiO_2, where it behaves compatibly. Amphiboles from Stage IV are typically the most potassic (Bewick, 2016), and biotite is also observed in these lavas suggesting that the appearance of these phases on the liquidus could explain this inflection, and similar infections seen with Rb and Ba. Finally, P_2O_5 behaves compatibly, presumably due to apatite crystallising, except in the Gudauri Formation, which have SiO_2 lower than the apatite saturation point, which based on the inflection point (Fig. 7h) is at ~59 wt % SiO_2.

The major element data (Fig. 6) are consistent with crystallisation of the phenocryst assemblages and do not define a single liquid line of descent, but rather suggest that are two distinct groupings in the lava suites, which may reflect different melting and fractionation histories. Lavas from the Gudauri Formation and Mt. Kazbek Stage IV have similarities in the major element chemistry generally having lower Na_2O and higher K_2O and Al_2O_3 for a given SiO_2 compared to other lava groups. They also contain high-Al pyroxenes (Table 1), which may represent crystallisation at higher pressures (Putirka, 2008), consistent with a different crystallisation history to the other lavas. These differences are also clear in the middle to HREE content (e.g. Dy/Yb ratio) of these two lava groups and in their Pb isotope data (see Fig. 11b).

To explore the differences between the lava groups with respect to their MREE to HREE contents and to determine how they might be utilised to understand mantle melting, it is important to consider the effects of crystal fractionation. This is particularly true for continental arc rocks because they fractionate amphibole, but also because some Greater Caucasus lavas contain high-Al pyroxenes. Both clinopyroxene and amphibole preferentially host MREEs significantly over LREEs and to a lesser extent over HREEs (Davidson *et al.*, 2007), producing concave down REE profiles (Davidson *et al.*, 2013). Fractionation of both clinopyroxene and amphibole can have a similar effect, but as $Kd_{amph} > Kd_{cpx}$ (Davidson *et al.*, 2007) for MREE, amphibole is likely to be the dominant cause of variation, but it is important to consider the high-Al clinopyroxenes. REE partitioning of amphiboles changes as the magmatic system becomes more

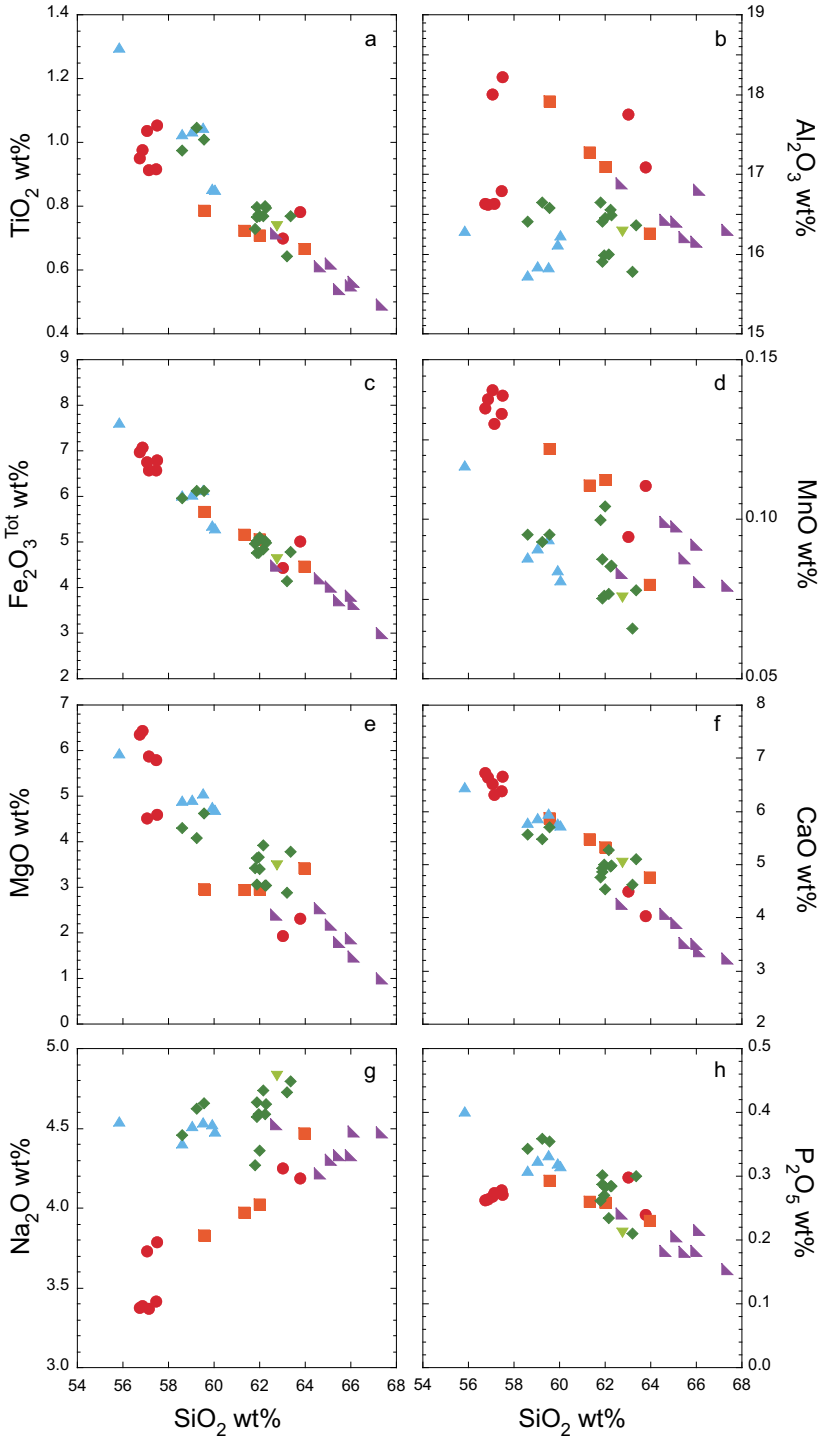

Fig. 6. Major- and minor-element data for lavas from the Mt. Kazbek region plotted against SiO_2. Symbols are the same as Fig. 6 and 2se uncertainties are smaller than symbol size.

evolved, with both the absolute values of partitioning REE coefficients and the relative MREE/HREE partitioning ratio increasing (e.g. Sisson, 1994). Clinopyroxene REE partitioning is sensitive to the Al and Na content of the pyroxene (Wood & Blundy, 1997; Blundy *et al.*, 1998). Although Dy/Yb partitioning is approximately unity in clinopyroxene, high-pressure aluminous clinopyroxenes can have Dy/Yb partitioning less than unity, with Yb being compatible (Blundy *et al.*, 1998). Therefore, the absolute abundance of Dy and Yb during fractionation also needs to be considered along with Dy/Yb.

Figure 12a illustrates how $[Dy/Yb]_N$ covaries with SiO_2 for the various lava groups. Groups I–III and the Qabarjina Formation define trends whereby $[Dy/Yb]_N$ smoothly decreases with increasing SiO_2, whereas Yb contents are relatively constant (Fig. 7f), consistent with amphibole ± plagioclase and pyroxene fractionation, although it should be noted that Group II and III lavas

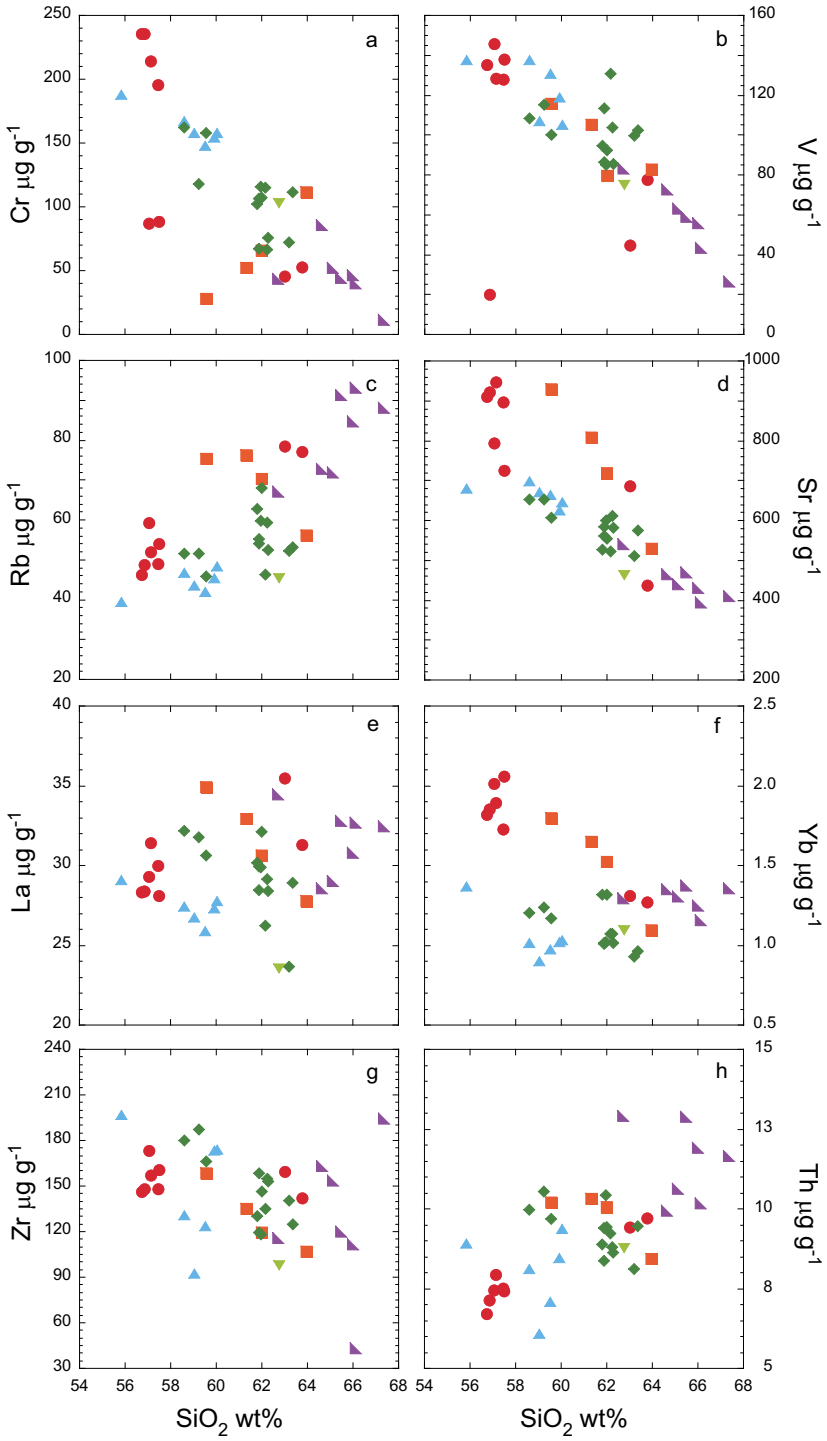

Fig. 7. Selected trace element for lavas from the Mt. Kazbek region plotted against SiO_2. (a) Cr, (b) V, (c) Rb, (d) Sr, (e) La, (f), Yb, (g) Zr and (h) Th.

with less than 59 wt % SiO_2 have relatively constant $[Dy/Yb]_N$ ratios of ~1.68, which requires a reduced role for amphibole in the least evolved samples. Gudauri Formation and Mt. Kazbek Stage IV have relatively constant $[Dy/Yb]_N$ ratios of ~1.28 except at high SiO_2 where the ratio increases to ~1.55, while the Yb content drops throughout fractionation (Fig. 7f). These data are consistent with both amphibole and high-Al pyroxene ± plagioclase crystallising. The increase in $[Dy/Yb]_N$ in the evolved compositions is hard to reconcile with crystallisation of any observed phenocrysts, but rather might record the removal of amphibole via melt reaction or mixing with evolved melt composition similar to the Qabarjina Formation (Fig. 12a), which is consistent with Pb isotopic data. What is clear is that the $[Dy/Yb]_N$ ratio in the evolved samples is modified by fractionation and that the Mt. Kazbek region is fed by distinct high and low $[Dy/Yb]_N$ melts. This point is also emphasised in Fig. 12b,

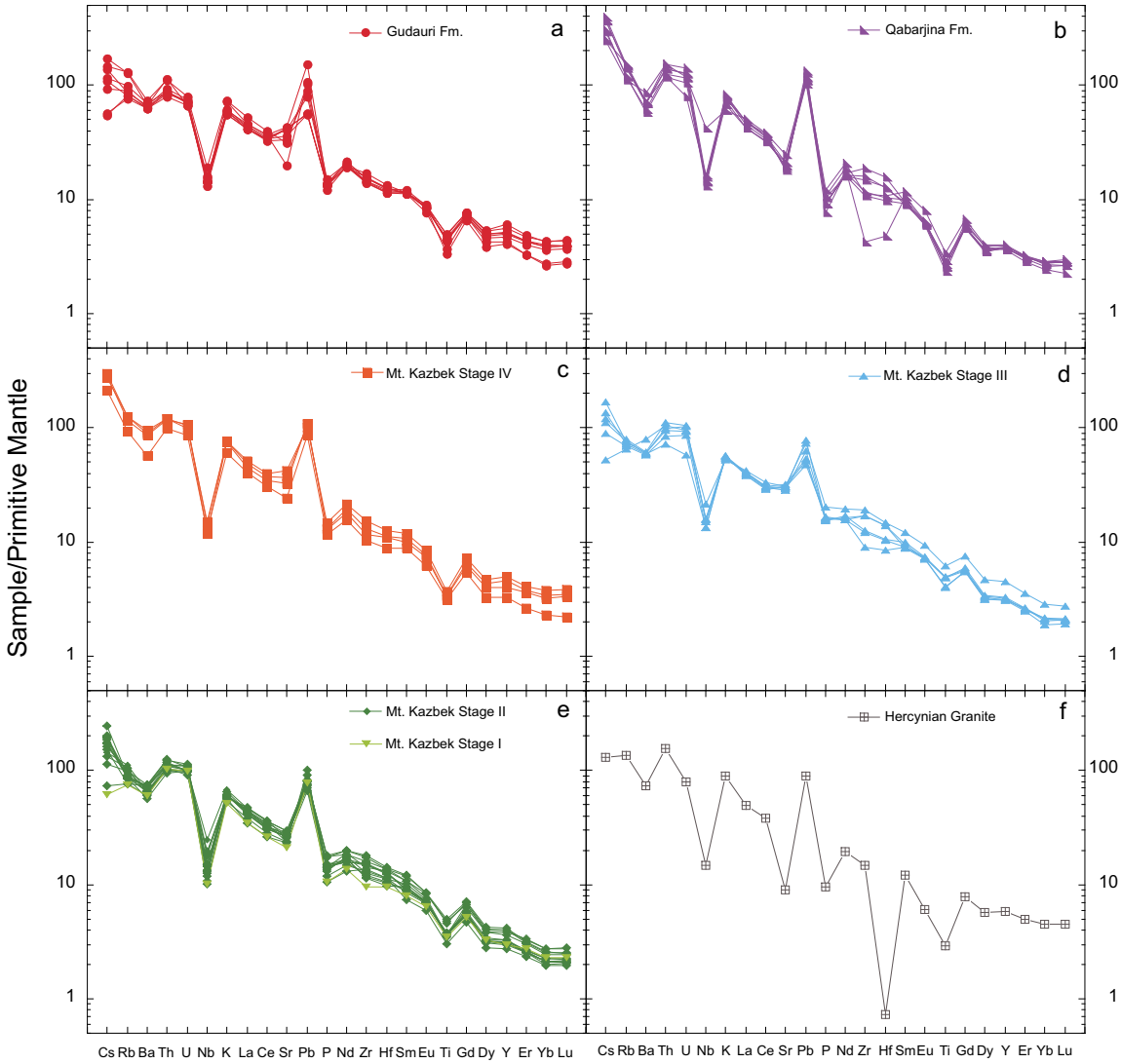

Fig. 8. Primitive-mantle normalised trace element plots for lavas from the Mt. Kazbek region (a–e) and a representative Hercynian Granite (f) that makes up part of the exposed basement close to Mt. Kazbek. Normalising values are from Palme & O'Neill (2014).

which illustrates that Th/Yb correlates well with SiO_2, indicating it is controlled by fractional crystallisation, but defines two broad groups, which must have had different primary Th/Yb ratios.

In conclusion, it is not surprising that there is no single liquid line of descent that describes all of the data given the lavas in this study were erupted over a 450 Ka time period. However, major and trace element data suggest that various lava groups can be described by two different liquid lines of descent reflecting two different primary liquids.

Crustal contamination

Crustal contamination has been suggested to play a role in the petrogenesis of magmas from Eastern Turkey (Keskin *et al.*, 1998), the Lesser Caucasus (Neill *et al.*, 2013, 2015; Sugden *et al.*, 2019), Mt. Elbrus (Lebedev *et al.*, 2010; Chugaev *et al.*, 2013) and the magmatic centres of Chegem and Tyrnyauz (Bindeman *et al.*, 2021). Therefore, it seems unlikely that lavas in the Mt. Kazbek region could have passed through greatly thickened crust (>60 km) without some crustal interaction. Crustal xenoliths are present in at least one flow from Stage II. This xenolith has a similar appearance to Hercynian granite exposed <20 km away (e.g. sample 13-021), suggesting that such material might be a potential crustal contaminant. Investigation of Sr–Nd isotopes (Fig. 10) indicates that lavas from the Mt. Kazbek region have compositions that lie within the mantle array, as do the majority of the lavas from the Lesser Caucasus whereas those from Mt. Elbrus are displaced to more radiogenic Sr isotope values. Previous studies indicate that crustal contamination is minimal within the Lesser Caucasus lavas (Neill *et al.*, 2013, 2015; Sugden *et al.*, 2019), whereas Lebedev *et al.* (2010) suggest that crustal contamination plays a significant role in modifying the composition of lavas from Mt. Elbrus. Similarly, Pb isotopic data for Mt. Elbrus, particularly $^{207}Pb/^{204}Pb$ ratios, indicate some contamination with local Greater Caucasus crust (Chugaev *et al.*, 2013).

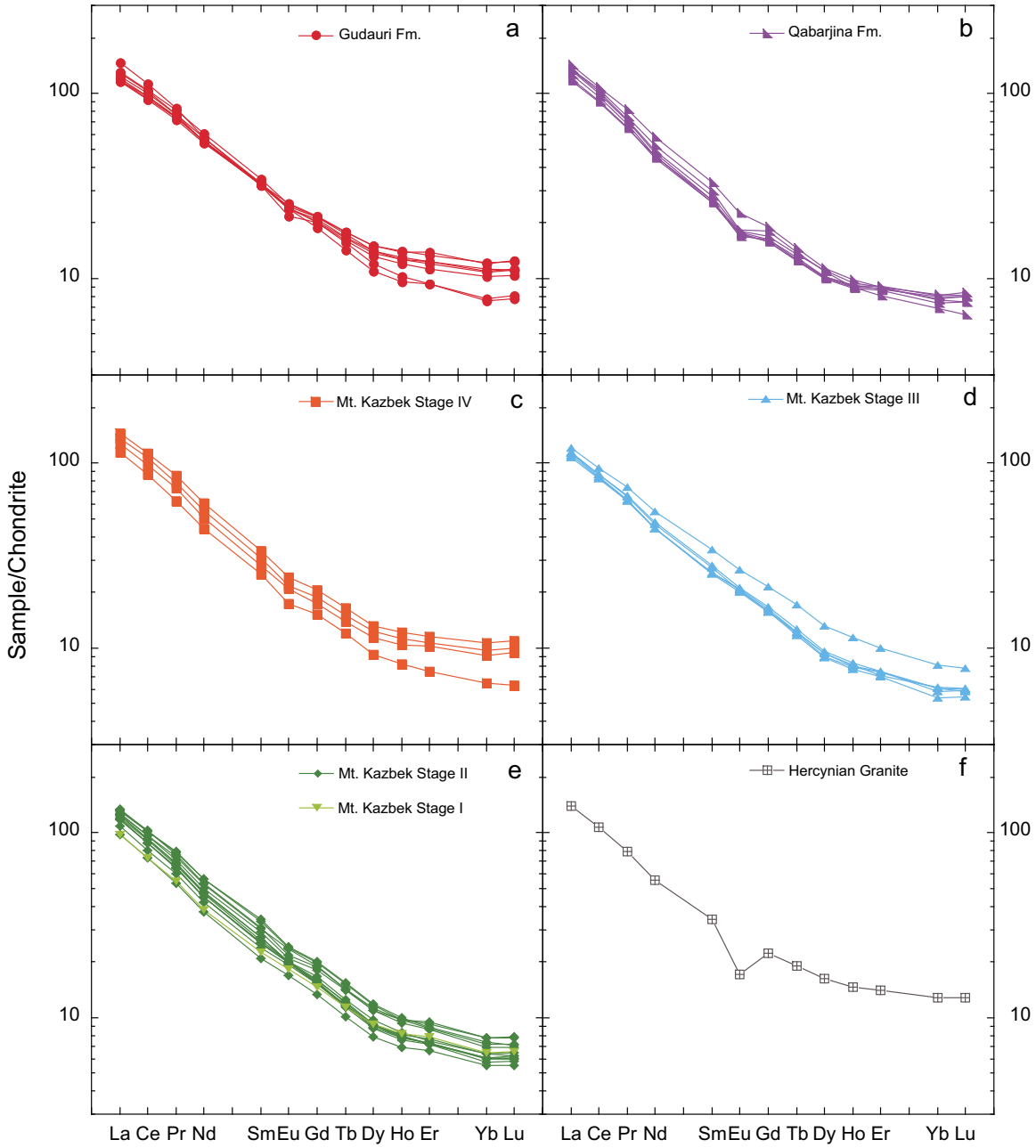

Fig. 9. Chondrite-normalised REE plots for lavas from the Mt. Kazbek region (a–e) and a representative Hercynian Granite (f). Normalising values are from Palme & O'Neill (2014).

To assess the role of simultaneous AFC isotope ratios are plotted against SiO_2 (Fig. 13). The correlations are scattered for Nd and Pb isotopes, with only $^{87}Sr/^{86}Sr$ having a broad positive correlation with SiO_2, although there is little systematic behaviour within individual lava groups, with some variation in all of the isotopes at similar SiO_2 contents for a given group. This observation makes modelling of AFC processes of limited use in providing quantitative constraints on crustal contamination. However, some qualitative observations can be made. Lavas from the evolved Qabarjina Formation have the most radiogenic Sr and least radiogenic Nd isotopes and their relatively low Sr and Nd contents make them most sensitive to contamination. They could be reasonably modelled using AFC equations to have been contaminated with the local Variscan granitic crust such that they increase their $^{87}Sr/^{86}Sr$ by 0.0007 from the most unradiogenic lava we measured with small assimilation/crystallisation rates (see DePaolo, 1981, for AFC model). By contrast, to increase from least to the most radiogenic Gudauri Formation, lava would require excessive amounts of crustal assimilation, inconsistent with its bulk chemistry. It should be noted that Parfenov *et al.* (2019) have suggested that Jurassic sediments from the Mt. Kazbek region could be a potential candidate for a crustal contaminate, but although they have elevated $^{87}Sr/^{86}Sr$ ratios (0.718621), their low Sr content (80 $\mu g\ g^{-1}$) would again require large

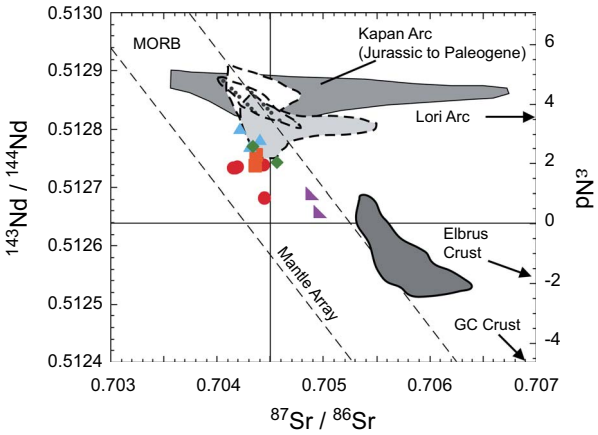

Fig. 10. Radiogenic neodymium versus strontium isotope data for the Mt. Kazbek region plotted with fields for Lesser and Greater (GC and Elbrus) Caucasus region lavas. Arrows point to local crustal material for each of the regions, all of which lie off the plot. Fields for the Kapan Arc from Mederer *et al.* (2013) and Lori Arc from (Neill *et al.*, 2015). The mantle array is from Zindler & Hart (1986) and the Bulk Silicate Earth (horizontal and vertical lines) is from Workman & Hart (2005). Symbols, fields and data sources are the same as Fig. 5 and 2se uncertainties are smaller than symbol size.

amounts of crustal assimilation inconsistent with our observations.

In Pb-isotope space (Fig. 11), the lavas define well-resolved positive linear trends, albeit over a limited range of $^{206}Pb/^{204}Pb$. The three Variscan Granite samples that we measured for Pb isotopes have more radiogenic compositions than the lavas, but contrasting $^{206}Pb/^{204}Pb$ and $^{208}Pb/^{204}Pb$ ratios compositions (they plot off Fig. 11 in the direction of the GC crust arrows). The linear variation in Pb isotopes could be explained by assimilation of the granitic basement but the basement has similar to lower Pb concentrations to the lavas and so any assimilation would produce small variations in the Pb isotopes of the lavas. In contrast to Sr and Nd isotopes, the evolved Qabarjina Formation does not have the most radiogenic Pb isotopes as would be expected for a simple AFC model. An alternative model for crustal contamination in continental arcs with thickened crust is the melting, assimilation, storage and homogenisation (MASH) model of Hildreth & Moorbath (1988), where there is no expectation of a relationship between radiogenic isotopes and SiO_2. This model can be explored by considering the relationship between Th/Yb and Pb isotopes, both of which are elevated in the Hercynian Granites. There is no positive relationship between Th/Yb and Pb isotopes (not shown), although each lava group having a distinct Th/Yb ratio (see Fig. 12b). Therefore, it could be argued that the MASH process sets the Th/Yb ratio. To test this, one can consider two potential end-member compositions for uncontaminated lavas being the least radiogenic Pb isotope values found for the Mt. Kazbek region or a melt produced by melting of a depleted MORB mantle (DMM)-like mantle. In the first case, small amounts of assimilation could produce the variation in the Pb isotopes, but it would have limited effect on Th/Yb and other key trace element ratios indicative of a subduction-zone modified source (e.g. Ba/Th, Nb/Nb∗). In the second model, the Pb isotopes can be reproduced but would not produce any of the key trace element ratios observed in the lavas. Therefore, while we cannot completely exclude some small shifts in the Pb isotope composition due to crustal contamination, neither an AFC- nor a MASH-type model fits the data. We suggest below there are other models for generating the Pb isotopic variation.

Overall, we conclude that there is some evidence for minor crustal contamination, but it is restricted to slightly increasing the $^{87}Sr/^{86}Sr$ of some evolved lavas and that the isotopic and trace element composition of the lavas provides insights into the composition of the mantle source.

Chemical nature of the source region

Trace elements

The trace element patterns for the lavas from the various centres of the Greater Caucasus are typical of arc lavas, in that they contain positive and negative anomalies compared to the smooth primitive-mantle normalised pattern expected for MORB and OIB. Key observations from the multi-element variation diagrams (Fig. 8) are negative anomalies in HFSEs (Nb and Ti) relative to LILEs and LREEs, although not in Zr, and enrichment in fluid-mobile elements such as Pb, Ba, Cs and Sr and a striking enrichment in Th. We have already demonstrated that crustal contamination does not produce the distinctive trace element signatures found in these lavas. In terms of understanding the origin of these trace element signatures, we will also compare the composition of the lavas in this study with those from the Lesser Caucasus because there may be common mantle and/or subducted components to both localities.

Modern arc systems can be divided into 'fluid dominated' and 'sediment dominated' by using key trace element ratios (e.g. Elliott, 2003; Plank, 2005). Fractional crystallisation has limited effect on the Ba/Th ratio and slightly increases $[La/Sm]_N$, but Fig. 14a illustrates that lavas from the Caucasus have a clear 'sediment dominated' signature, characterised by relative enrichment in Th and the LREE and that the source of the lavas has to be LREE-enriched relative to DMM and the primitive mantle. We can further assess trace-element enrichment by using plots of immobile trace element ratios, such as Th/Yb, Zr/Yb and Nb/Yb (Pearce and Peate, 1995; Pearce, 2008). Arc lavas define an array in Th/Yb versus Nb/Yb space that sits at elevated Th/Yb compared to the MORB–OIB array (Pearce, 2008). Additionally, continental arc rocks have enriched composition, with Nb/Yb ratios greater than 1. The Mt. Kazbek region data not only sit above the MORB–OIB array but also plot at elevated Th/Yb ratios compared with most continental arc rocks including the rocks from the Lesser Caucasus (Fig. 14b), suggesting these rocks have significant Th enrichment. Most continental arc rocks sit in the enriched portion on a Zr/Yb versus Nb/Yb plot

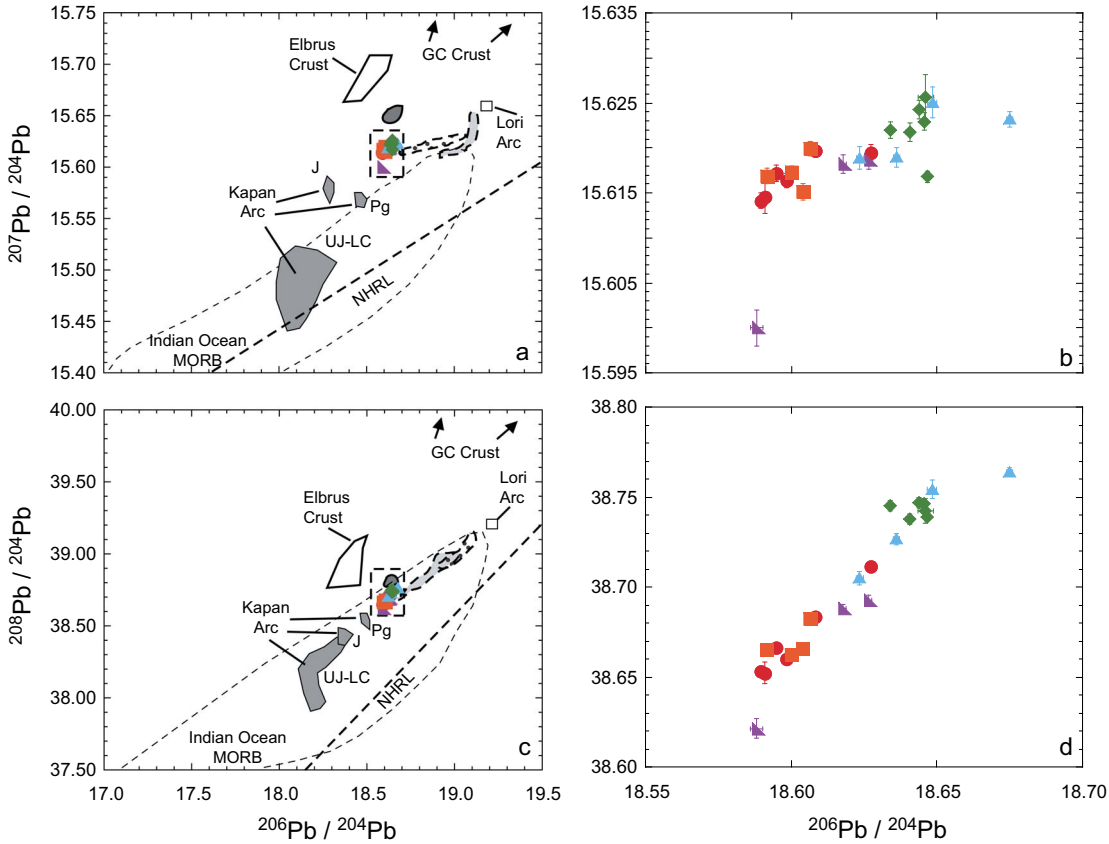

Fig. 11. Radiogenic Pb isotope data for the Mt. Kazbek region plotted with fields for Lesser and Greater Caucasus region lavas. (a) and (b) $^{207}Pb/^{204}Pb$ versus $^{206}Pb/^{204}Pb$ and (c) and (d) $^{208}Pb/^{204}Pb$ versus $^{206}Pb/^{204}Pb$. In (a) and (c) Greater Caucasus data are from Chugaev *et al.* (2013). Fields for the Kapan Arc from Mederer et al (2015) (where UJ is Upper Jurassic, LC is Lower Cretaceous, J is Jurassic and Pg is Paleogene) and Lori Arc from (Neill *et al.*, 2015). Arrows point to local crustal material for the Mt. Kazbek region, which lie off the plot (GC). Northern hemisphere reference line (NHRL) is from Hart (1984). Symbols, fields and data sources are the same as Fig. 5b. (d) Represents a close up of the Mt. Kazbek data (area is illustrated by dotted rectangular box in a and c). Where 2 se uncertainties are larger than the symbols they are illustrated as error bars.

(Fig. 14c) relative to rocks from depleted sources such as MORB (Pearce *et al.*, 1990) and this is true for the Greater Caucasus lavas. These plots clearly show that the Gudauri and Group IV lavas plot separately from the other lava groups and that the most primitive Group II and III lavas sit slightly above the depleted-enriched array and lavas from the Lesser Caucasus, a feature that is consistent with addition of slab-derived silicic melts (Pearce and Peate, 1995).

Source enrichment prior to melting is the most likely explanation of the multi-element pattern, with slab-derived fluids the most likely metasomatic agent, which requires a slab to have been present beneath the Greater Caucasus, or that subduction-zone enriched lithosphere has survived for some considerable time following initial collision. Slab-derived silicic melts, or super-critical fluids at depth, result in enrichment of all elements, even HFSEs and HREEs that are not enriched by simple H_2O-rich dehydration and the production of aqueous fluids (Kessel *et al.*, 2005). The super-critical fluids refer to fluids released after the critical endpoint and this may occur at depths as shallow as 100 km (Mibe *et al.*, 2011) or as deep as 180 km (Kessel *et al.*, 2005). However, water released from dehydration in the deep basaltic and ultramafic portions of the slab can trigger fluid-present partial melting within the trace-element enriched, sedimentary part of the slab (Hermann *et al.*, 2006), which can produce a similar signature to that seen in the lavas analysed in this study. Specifically, the lavas in this study have large negative HFSE anomalies and enrichment in Th and Zr. Negative HFSE anomalies can be the result of residual HFSE-bearing minerals left in the slab after dehydration processes, or as relics of dehydrated sediment (Hermann & Rubatto, 2009). Addition of Th and Zr requires melting beyond allanite-out and zircon-out, respectively (Hermann & Rubatto, 2009; Skora & Blundy, 2010), which requires relatively high degrees of melting of sediments within the slab. One scenario for producing these trace element signatures is that a subducted slab beneath the Greater Caucasus has been extensively heated by upwelling asthenosphere producing extensive melting of sediments within the slab.

Isotopes

Trace element data strongly suggest an enriched source for the lavas, similar to those found in modern arc settings and therefore the isotopic composition should provide further insight into the origins of this source. The

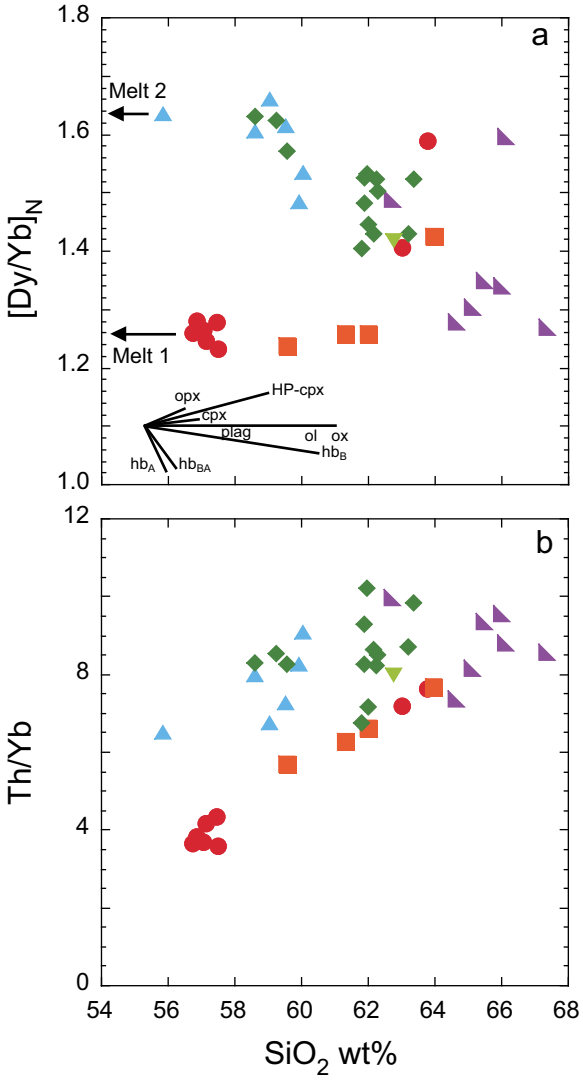

Fig. 12. Plots of (a) $[Dy/Yb]_N$ and (b) Th/Yb versus SiO_2 for the Mt. Kazbek region lavas. Melt 1 and Melt 2 represent the proposed $[Dy/Yb]_N$ of two distinct primary melts. Crystal fractionation vectors in (a) calculated using partitioning data from Sisson (1994), Wood & Blundy (1997), Blundy *et al.* (1998) and Wood & Blundy (2003) and mineral chemistry data from Bewick (2016). Vectors represent 30% crystallisation, except for oxide (10%) and plagioclase (50%), but will vary slightly depending on composition of initial melt. Abbreviations are olivine (ol), orthopyroxene (opx), clinopyroxene (cpx), high-pressure clinopyroxene (HP-cpx), plagioclase (plag), oxide (ox), amphibole crystallising from a basalt (hb_B), amphibole crystallising from a basaltic andesite (hb_{BA}) and amphibole crystallising from an andesite (hb_A).

isotopic composition of intra-oceanic arc lavas is thought to be controlled by the composition of the mantle wedge, which is assumed to have a DMM composition, a slab component with contributions from the subducted oceanic plate, which are thought to be dominated by dehydration fluids from various depths with the oceanic crust and a melt/fluid component from the subducted sediment. For a given arc system, there is usually enough geochemical data to have reasonable constraints on the composition of these components. By contrast, the geodynamics of the Greater Caucasus make it harder to estimate these input parameters. The mantle wedge could be relatively young Eurasian mantle lithosphere or lithosphere associated with the Trans-Caucasian back-arc basin. Subducted slabs of oceanic crust from the Palaeo-Tethys and Trans-Caucasian back-arc basin potentially sit underneath Mt. Kazbek, and both plates could carry Tethyan margin sediments. Finally, any potential asthenospheric component (i.e. upwelling due to lithospheric delamination) most likely has affinities with Indian MORB mantle.

Previous studies on post-collision volcanics in the Lesser Caucasus from Iran (Allen *et al.*, 2013) and Armenia (Sugden *et al.*, 2019) have modelled the Sr and Nd isotope composition of these lavas by mixing DMM (from Workman & Hart, 2005) with two potential subducted sedimentary compositions: the global average subducted sediment from Plank & Langmuir (1998) and a sandstone sample from a Tethyan flysch sequence (Prelević *et al.*, 2008) that is potentially representative of subducted sediment on the Tethyan plate. We have produced similar mixing calculations, which are illustrated in Fig. 15a. Previous studies (e.g. Sugden *et al.*, 2019) find the bulk mixing models plot close to the lava compositions but always lie at Sr isotope composition that is too radiogenic for a given $^{143}Nd/^{144}Nd$. This issue is compounded for the Mt. Kazbek region samples because these data generally plot further to the left in the mantle array at lower $^{87}Sr/^{86}Sr$ ratios than samples from the Lesser Caucasus. Moreover, the modelling in the previous papers used the least radiogenic composition of the Tethyan sediments from Prelević *et al.* (2008), whereas using an average value pushes the curve further from the data (Fig. 15a). A more realistic approach than bulk mixing of the sediment would be to add a sediment melt from the putative slab to the mantle wedge. Using appropriate bulk distribution coefficients from Skora & Blundy (2010), the effect is simply to increase the Sr/Nd ratio of the melt relative to the bulk sediment, but the mixing curves still miss the data. Finally, the choice of DMM as the mantle end-member may be incorrect, and a more enriched source such as E-DMM (Workman & Hart, 2005) places the mixing curves slightly closer to the data.

Simple binary mixes between a mantle and slab component do not fit the data and are inconsistent with modern views on Sr and Nd isotopic systematics in arc systems (e.g. Elliott, 2003). In any mantle source that has been modified by subduction-zone input, the Sr can be sourced from the mantle wedge, subducted sediment, altered oceanic crust (AOC) and fluid from the deeper portions of the subducted slab. Therefore, we can assess whether the source of the Kazbek lavas is consistent such a subduction-zone origin. A useful way to forward model the mixing of these components is via simple mass balance equations and a Monte Carlo model, in which the proportion of Sr from the four components can be varied. The advantage of this type of modelling is that it does not require the Sr and Nd concentrations of the components. We follow the methodology of Klaver *et al.* (2020) using an appropriate range of compositions for the components

(see Table 3). We ran ~10^6 models and a successful run reproduces the Sr and Nd isotope and Sr/Nd ratios of the Kazbek lavas (excluding samples from the Qabarjina formation, which are the most evolved and thus, potentially, their Sr isotope compositions have been slightly modified by crustal contamination). Results from the modelling indicate the following proportions from each of the components; mantle wedge (0.154), subducted sediment (0.109), AOC (0.133) and fluid (0.604). The results indicate that the Sr budget is controlled by fluids from deeper within the subducted slab, which have less-radiogenic Sr isotope ratios. These results are consistent with other arc systems, including those that have 'sediment dominated' trace element signatures (Klaver *et al.*, 2020). Implicit in these results is that the trace element signature of the Mt. Kazbek region lavas requires significant input from a subducted slab, with deep-sourced fluids fluxing the slab, although the timing of this enrichment is not constrained by the modelling.

The least radiogenic Pb isotopic data for the Mt. Kazbek region lavas lie between recent volcanic rocks from the Lesser Caucasus (Neill *et al.*, 2013, 2015) and lavas from the middle Jurassic to Cenozoic Kapan arc in southern Armenia (Mederer *et al.*, 2013). Neill *et al.* (2013, 2015) ascribe the trend in the Lesser Caucasus data to lower $^{206}Pb/^{204}Pb$ as being related to AFC processes whereby pre-existing arc crust from the Kapan arc is assimilated during magma transport. Such a process is unlikely to explain the composition of the Mt. Kazbek region lavas given its position much further north within the collision zone. However, plots of $^{207}Pb/^{204}Pb$ and particularly $^{208}Pb/^{204}Pb$ versus $^{206}Pb/^{204}Pb$ indicate that regressions through the Mt. Kazbek and Lesser Causasus data meet at a common Pb isotopic composition with a $^{206}Pb/^{204}Pb$ of 18.6, $^{207}Pb/^{204}Pb$ 15.60–15.61 and $^{208}Pb/^{204}Pb$ of 38.6 (Fig. 15b). The most likely explanation of this is a common lithospheric source for both suites of lavas. This common source can be explained by either a long-standing mantle source similar to the Kapan arc that has evolved to more radiogenic Pb isotope composition through the Cenozoic or subduction of arc material from the Kapan arc beneath the modern day Caucasus that has then enriched the mantle source. We demonstrate in the next section that the Mt. Kazbek magmas were produced by small degrees (3–5%) of partial melting, which allows us to estimate U/Pb and Th/Pb ratios of the mantle source using appropriate partitioning coefficients. This yields values for U/Pb ~0.148 and Th/Pb of ~0.642, which over time allows the evolution of a Kapan type mantle to produce an enriched lithospheric source with Pb isotopic compositions consistent with the Lesser and Greater Caucasus data (Fig. 15b).

By contrast with the Lesser Caucasus data, the Mt. Kazbek region lavas also plot away from this common Pb isotopic composition towards a sedimentary component consistent with the mean Tethyan flysch composition of Prelević *et al.* (2008). This is consistent with the Pb budget of many arcs being dominated by slab inputs (e.g. Kessel *et al.*, 2005) and that a compositionally distinct sediment source resides beneath the Greater Caucasus, producing characteristic trace element and Pb isotopic signatures. In detail, Tethyan sediments analysed by Prelević *et al.* (2008) are 80 My old and therefore represent a potential sediment component that could have been subducted over this time period. Modelling of Sr–Nd isotopes presented in previous studies (e.g. Sugden *et al.*, 2019) uses a composition that is 80 Ma in their mixing models, although the modelling is not particularly sensitive to the age. By contrast, the Pb isotope systematics illustrated in Fig. 15b demonstrates that the Lesser Caucasus data are inconsistent with mixing these Tethyan sediments at any time over the past 80 Ma. Critically, the Mt. Kazbek data plot towards a Tethyan sediment composition that may have been added to the mantle during the past 10 Ma. We conclude that a subduction-zone modified lithospheric source is present across the Caucasus, although the proportion and timing of inputs may vary across the region. Moreover, Sr, Nd and particularly Pb isotopic data for Mt. Kazbeg are inconsistent with simple mixing between the common Caucasus mantle composition of Lebedev *et al.* (2014) and local continental crust.

Partial melting model

Trace element and isotopic systematics indicate that the lavas from the Mt. Kazbek region were derived from melting a source with a LREE-enriched composition. This is most likely a lithospheric source that had been modified by melts and/or fluids from material subducted before and through the collisional event. Potential candidates for the lithospheric source include both fertile and depleted mantle that is variably enriched with easily fusible pyroxenitic veins and/or mantle that contain hydrous phases such as amphibole or phlogopite. It is difficult to compare mantle-melting models across the Greater Caucasus, as the silicic melts from the western part of the range are masked by significant amounts of crustal input. By contrast, modelling of Lesser Caucasus lavas has concluded that in SW Armenia some melting occurred at depths that required garnet to be a residual phase (Sugden *et al.*, 2019), whereas in Central and NW Armenia melting is shallower and restricted to the spinel-peridotite facies, although a depleted source (an amphibole-bearing harzburgite) has been invoked to be the source of some of the lavas from Yerevan (Central Armenia) (Neill *et al.*, 2015).

REEs are particularly useful for understanding melting of the mantle, because they are dependent on melt fraction, source composition and source mineralogy, particularly the ratio of MREE to HREE (e.g. Dy/Yb), which is sensitive to garnet and amphibole in the mantle source. Figure 16 illustrates a range of melting models plotted on the $[Dy/Yb]_N$ versus $[La/Yb]_N$ diagram. We have constructed melting curves for garnet- and spinel-peridotite melting and for a decompression melting path, where melting is initiated in the garnet peridotite facies and continues into the spinel-peridotite facies, with the

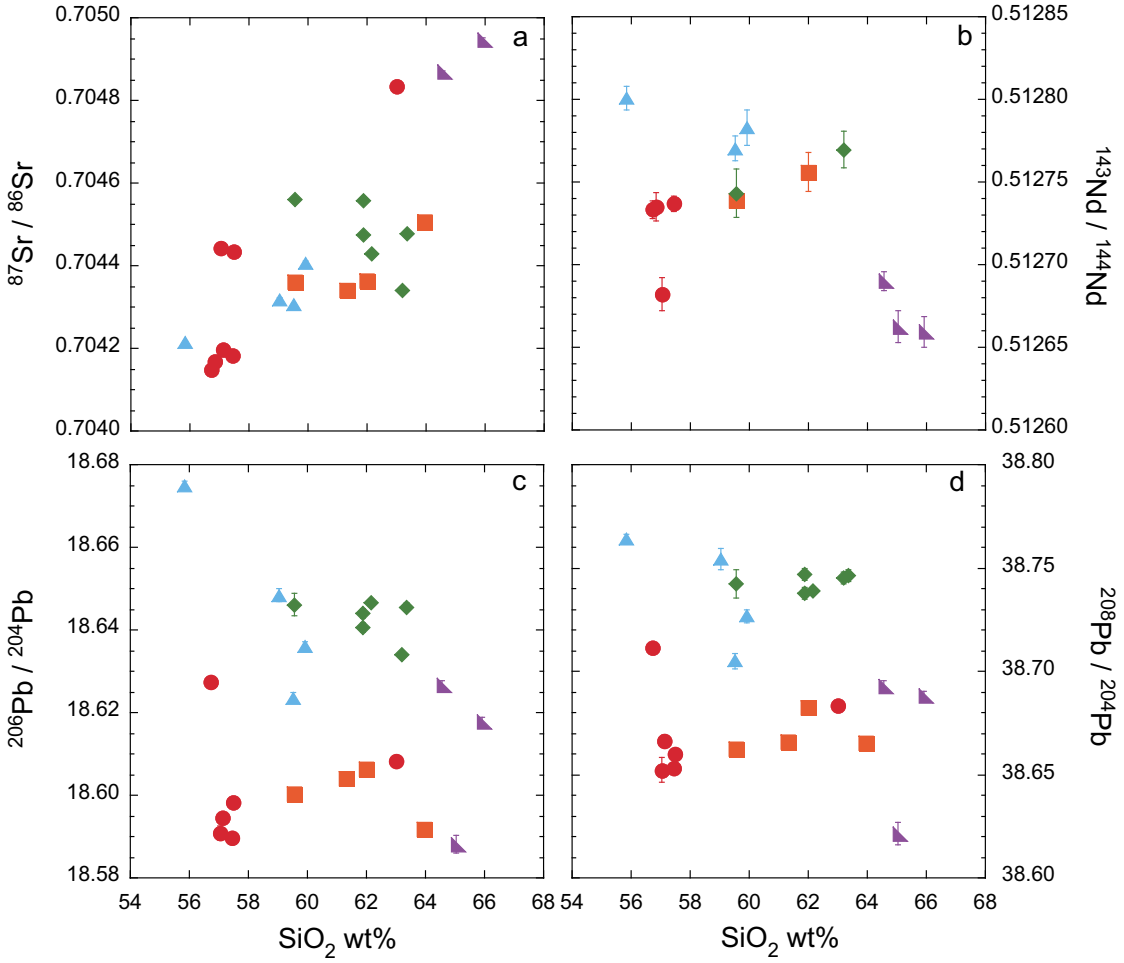

Fig. 13. Plots of radiogenic isotopic data versus SiO_2 for Mt. Kazbek region lavas. (a) $^{87}Sr/^{86}Sr$, (b) $^{143}Nd/^{144}Nd$, (c) $^{206}Pb/^{204}Pb$ and (d) $^{208}Pb/^{204}Pb$.

melts being pooled. Additionally, we have modelled the effects of melting an amphibole-peridotite and of garnet- and spinel-bearing pyroxenites (see figure caption for details of melting models). Trace element ratios such as La/Sm suggest the source is LREE-enriched (see Fig. 14a) and so we model the source of the lavas consistent with the La/Sm ratio (corrected from fractional crystallisation) to yield a source with a $[La/Yb]_N$ ratio of 2 and a $[Dy/Yb]_N$ of 1.

None of the melts in the this study is primary but the Mg# of the least evolved samples is ~65, suggesting that that they have undergone fractionation of mafic phases, most likely olivine and Cr-spinel that will not have significantly modified the REE ratios of interest. The least evolved Gudauri Formation and Kazbek Group IV lavas plot on or near to the spinel-peridotite melting curve. Their exact positioning of these lavas relative to the curve depends on how LREE-enriched the source is and on the melt fraction, but require small (<3%) degrees of partial melting to produce the shape of the REE pattern. The source region could accommodate a small amount of amphibole (~2%), but larger proportions would produce melts with too low $[Dy/Yb]_N$. In detail,

Table 3: Parameters used for Sr–Nd isotopic modelling*

Component	Prop. of Sr	$^{87}Sr/^{86}Sr$	$^{143}Nd/^{144}Nd$	Sr/Nd
DMM	0–0.3	0.7023–0.7028	0.5130–0.5132	13–15
Sediment	0–0.3	0.711203–0.71883	0.51211–0.512165	3.3–33.4
AOC	0–0.3	0.7039–0.7051	0.51312–0.51315	8.3–40
Fluid	0–1	0.7024–0.7040	0.51314	90–500

*Each column represents the range of each parameter that is allowed to vary randomly in each mixing simulation (see Klaver *et al.* (2020) for details). The proportion of Sr relates to the proportion of Sr contributed by each of the four components to the mixture. Compositions of these components are from the following sources; DMM (Workman & Hart, 2005), Tethyan sediment data (Prelević *et al.*, 2008) and AOC and Fluid (Klaver *et al.*, 2020).

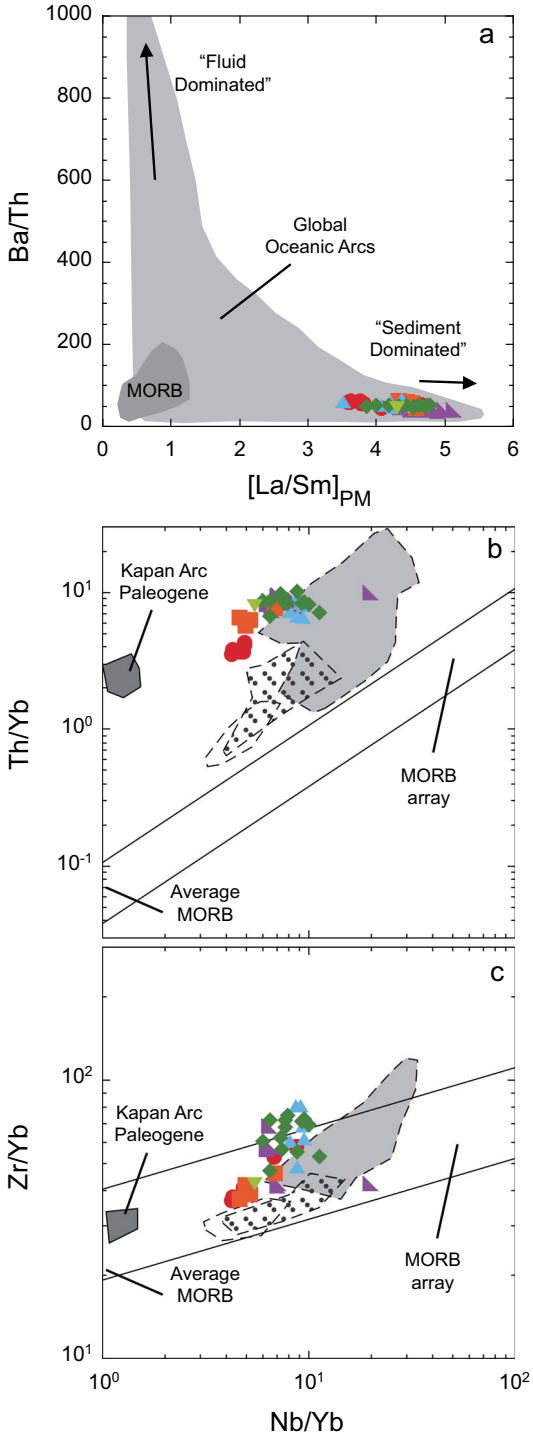

Fig. 14. Plots of (a) Ba/Th versus $[La/Sm]_{PM}$ (fields from Elliott, 2003), (b) Th/Yb versus Nb/Yb and (c) Zr/Yb versus Nb/Yb. MORB-array from Pearce & Peate (1995) and fields for Lesser Caucasus data are the same as those in Fig. 5.

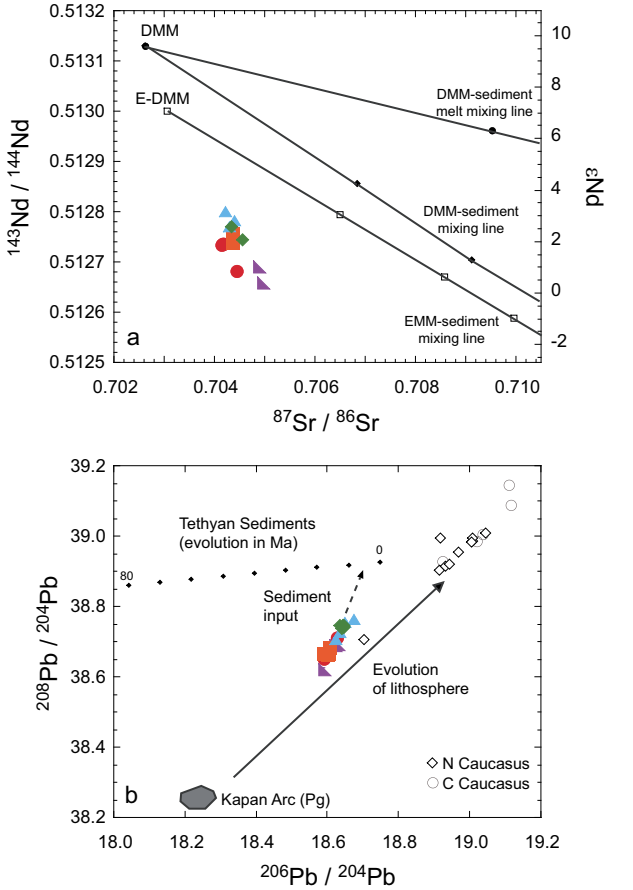

Fig. 15. (a) Radiogenic neodymium versus strontium isotope data for the Mt. Kazbek region. Also illustrated are three mixing curves. Two curves represent mixing between DMM and either bulk sediment or sediment melt of the average Tethyan sediment data from Prelević *et al.* (2008). Sediments melts are calculated using appropriate bulk distribution coefficients from Skora & Blundy (2010). The third mixing curve is between E-DMM and bulk-sediment. Symbols represent 10% increments in mixing. DMM and E-DMM are from Workman & Hart (2005). (b) $^{208}Pb/^{204}Pb$ versus $^{206}Pb/^{204}Pb$ for lavas from this study and Neill *et al.* (2013, 2015). Fields for the Kapan Arc from Mederer *et al.* (2015). Tethyan sediment data from Prelević *et al.* (2008), illustrating its evolution over the last 80 Ma (ticks represent 10 Ma intervals). Evolution of the Kapan Arc uses U/Pb of 0.148 and Th/Pb of 0.642, based on calculated source ratios for Mt. Kazbek lavas assuming 3–5% partial melting.

while the trace element ratios are consistent with melting in the spinel field, the modelled MREE–HREE abundances are too high compared with the lavas. This could be resolved by (1) melting of a slightly more depleted source or (2) slight compatibility of HREE in the aluminous clinopyroxene during the initial stages of melting in the spinel field (Robinson *et al.*, 1998). Immobile trace element contents such as Ti suggest that the source is not depleted and we prefer that the HREE contents are simply controlled by the mantle mineralogy and partitioning.

The least evolved of the Group II and III lavas from Mt. Kazbek have distinctly elevated $[Dy/Yb]_N$ ratios that require some melting in the garnet peridotite facies. Modelling of these lavas is consistent with melting starting in the garnet peridotite and continuing into the spinel facies or potentially lying in the garnet-spinel transition zone. It is not possible to distinguish between these processes, or to preclude the possibility that a small amount of amphibole is present in the mantle, but in any case the required melt fraction is 3–4%. We suggest small differences in the depth of melting are related to small differences in the thickness of the lithosphere.

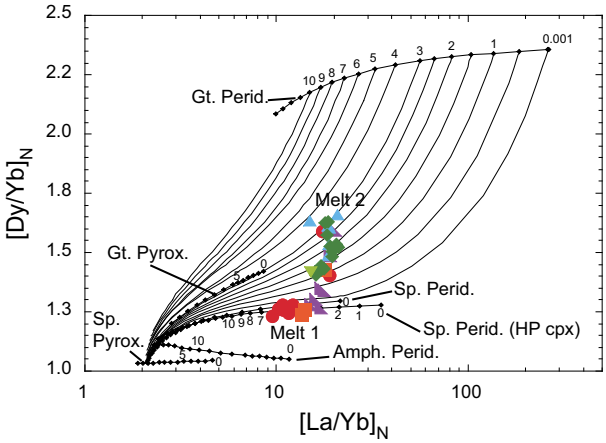

Fig. 16. Plots of $[Dy/Yb]_N$ versus $[La/Yb]_N$ for lavas from this study. Melt 1 and Melt 2 represent the composition of the two distinct primary melts. Dispersion between these two compositions is related to fractional crystallisation (see Fig. 12a). Garnet and spinel peridotite melting curves are joined by curved lines that represent pooled melts along decompression melting paths. Also shown are curves for spinel and garnet pyroxenite melting and amphibole peridotite melting. Partition coefficients from Hauri & Hart (1994) and McKenzie & O'Nions (1991). Melting modes from Hauri & Hart (1994) (spinel and garnet peridotite), McKenzie & O'Nions (1991) (amphibole peridotite) and Borghini *et al.* (2017) (spinel and garnet pyroxenite). See text for information about the source.

Trigger for mantle melting

The region of recent magmatism in the Greater Caucasus is coincident with the area of rapid young cooling, determined from recent thermochronometric studies (Vincent *et al.*, 2020), and enhanced exhumation during the Pliocene–Quaternary (Morton *et al.*, 2003; Avdeev & Niemi, 2011). Modelling of the thermochronometric data is consistent with buoyancy effects associated with mantle upwelling, with a wave-length of several 100 km. However, differences in lithospheric structure/composition may modulate the wavelength of exhumation, consistent with observations across the Greater Caucasus (Vincent *et al.*, 2020). The influence of mantle upwelling beneath regions of thickened lithosphere and its likely effects on magmatism have been considered by several studies (e.g. Pearce *et al.*, 1990). Factors that need explanation in the Greater Caucasus are (1) that magmatism is concentrated in regions of thickened crust, (2) that magmatism occurs ~30 Ma after the initial collision and (3) the potential for a remnant subducted slab beneath the mountain belt associated with either the Pontides or the Trans-Caucasian back-arc basin.

Viscosity contrasts caused by small amounts of H_2O in the asthenosphere (a few hundred μg/g H_2O) can result in small-scale convection, which can produce small delamination events (or drips) at the base of the lithosphere every few million years (Kaislaniemi *et al.*, 2014). Such events will allow asthenosphere to rise and produce small volumes of asthenospheric decompression melts or more importantly provide a heat source to the overlying lithosphere. The lithosphere will preferentially melt over the asthenosphere due to the higher water content, and its more fusible amphibole-rich mineralogy. In the Greater Caucasus, late Cenozoic lithospheric shortening and thickening (Morton *et al.*, 2003; Avdeev & Niemi, 2011) would have enabled drips to form, and, in combination with mantle upwelling, could produce volcanism over the thickest region of crust recognised in the Greater Caucasus.

Other proposed mechanisms for generating magmatism in the Arabia–Eurasia collision are slab break-off of the subducted oceanic plate beneath the collision zone (e.g. Omrani *et al.*, 2008) and wholesale delamination of the lower lithosphere (e.g. Pearce *et al.*, 1990). The slab break-off model has the general problem that unless break-off occurs at a very shallow depth, the thermal perturbation to the adjacent mantle takes place at too great a depth to cause melting that reaches the surface (Freeburn *et al.*, 2017). There is also a regional problem in that magmatism in the Arabia–Eurasia collision zone occurs as scattered centres across a vast area, initiated many millions of years after the initial continental collision, and without a discernible pattern in the location or composition of volcanic centres (Kaislaniemi *et al.*, 2014). This is different behaviour to that of recent magmatism in the Tibetan Plateau where spatial–temporal trends have been picked out from the age data (e.g. Law & Allen, 2020). Wholesale loss of the lower lithosphere faces a similar issue: why should a single, major, reconfiguration of the Eurasian plate produce such scattered magmatism across the width and breadth of the collision zone?

Figure 17 draws together recent seismic data, geodynamic constraints and observations on the geochemistry to produce a snapshot of what triggers melting in the Greater Caucasus. The geochemistry of the Mt. Kazbek region lavas is consistent with melting of mantle that has been extensively modified by subduction zone fluids and melts. Isotopic data suggest an underlying common lithospheric source to volcanism from across the Lesser and Greater Caucasus, but the lavas in the Mt. Kazbek region are produced from a source that is enriched, suggesting either a greater slab input or one that is different in composition compared to the Lesser Caucasus. Recent geophysical studies (e.g. Zabelina *et al.*, 2016) are hard to reconcile with a wholesale slab lying directly beneath Mt. Kazbek, but it is reasonably to propose that Transcaucasus oceanic basement material, including Tethyan sediments, is located within the collision zone and would provide a source for additional trace element enrichment. Additionally, we can identify two distinct geochemical lineages, with melting occurring at depths just below and just above the garnet-spinel peridotite transition, indicating some local lithospheric control on melting depth. Small-scale convection related to mantle upwelling provides a plausible mechanism for the Greater Caucasus magmatism during the late Cenozoic, while local lithospheric and crustal heterogeneity may explain the difference in composition between lavas erupted in in the Mt. Kazbek region and Mt. Elbrus (~170 km to the NW).

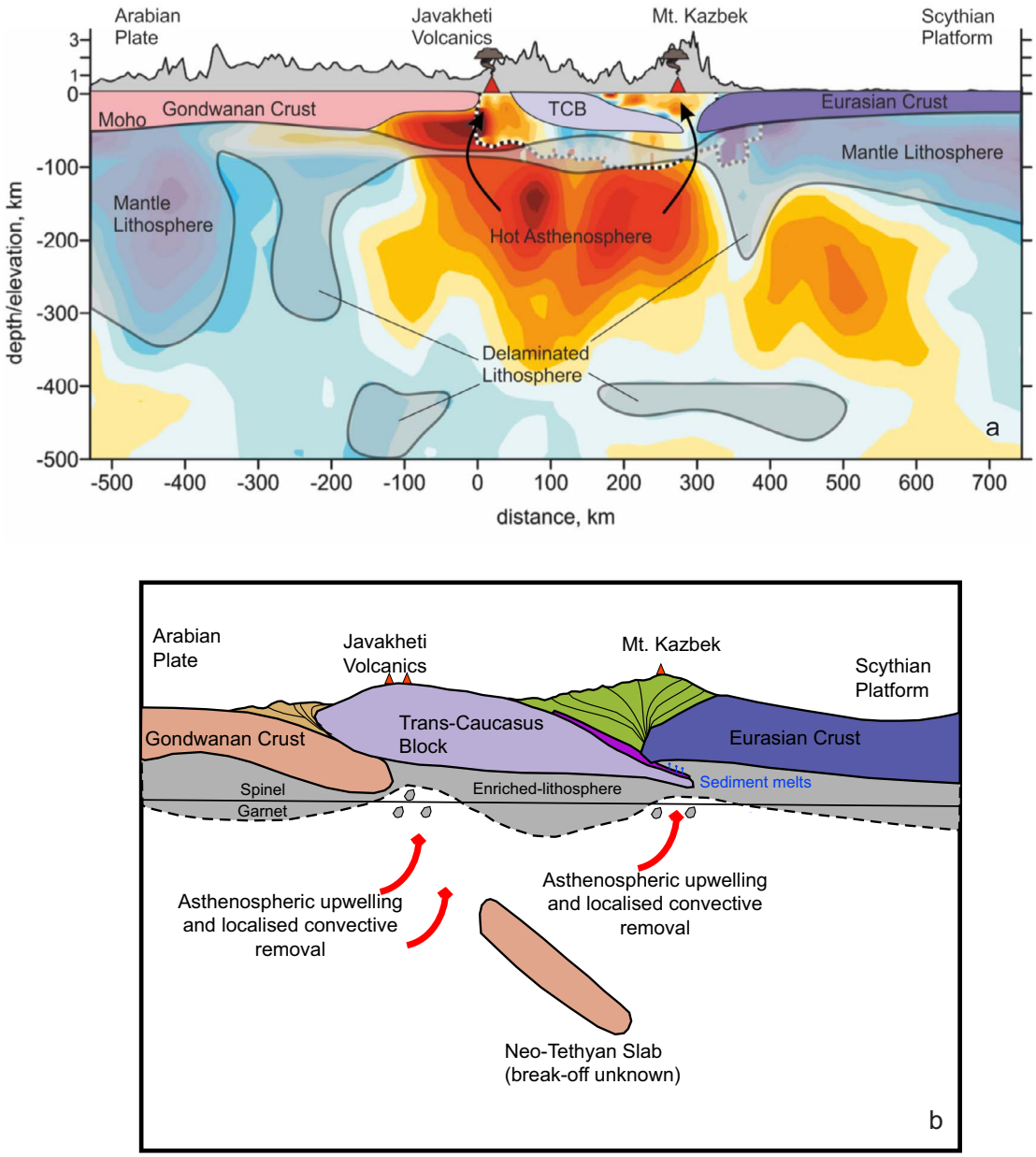

Fig. 17. (a) Thermal model of the Caucasus based on inversion of global International Seismological Centre (ISC data) and local P-wave anomalies (from Zabelina *et al.*, 2016). The interpretation of various crustal, lithospheric and asthenospheric domains is based on the work of Zabelina *et al.* (2016). (b) Schematic cross-section of geodynamic model for melt generation in the Greater Caucasus based on the previous work of Neill *et al.* (2013, 2015) for the Lesser Caucasus with further constraints provided by this study. The brown and green units represent rocks deformed due to continent collision. The purple unit represents Transcaucasus basement material including sediments that is a potential source for the addition trace element enrichment of the Mt. Kazbek magmas.

CONCLUSIONS

We have analysed Quaternary volcanic rocks from the Mt. Kazbek region, Georgia, in the central part of the Greater Caucasus. Samples are classified by age and location into three main groups: around Mt. Kazbek itself, and the nearby Gudauri and Qabarjina formations. The Mt. Kazbek volcanics are further divided into four stages (I–IV), corresponding with previous studies, field observations and age determinations (Lebedev *et al.*, 2014). The lavas are calc-alkaline in nature with compositions in the range of basaltic andesite to dacite (57–67 wt % SiO_2) and trace element patterns with a supra-subduction signature, with large negative Nb anomalies and enrichment in LILE, particularly Th. Although the lavas were erupted through thick continental crust, there is little evidence for extensive modification by crustal contamination. The lavas can be placed into two distinct groups, based on their mineralogy, trace element and Pb isotopic compositions. Furthermore, REE signatures for the two groups represent melting just above and below the garnet-spinel peridotite transition, suggesting some local lithospheric control on melting. In common with Quaternary post-collisional volcanic rocks across the Caucasus, a subduction-zone

related, fluid-enriched source remained intact after initial Arabia–Eurasia continental collision, although the trace element signature is more enriched in the Mt. Kazbek region (Fig 17.) with a characteristic sediment melting signature, which requires recent recycling of sediment into the source region beneath Mt. Kazbek during collision.

The Greater Caucasus volcanism is only a small domain of a much wider collection of late Cenozoic magmatic centres that has developed across the Arabia–Eurasia collision zone (Pearce *et al.*, 1990; Chiu *et al.*, 2013). Several mechanisms have previously been proposed for generating this magmatism: break-off of the Neo-Tethyan oceanic slab, wholesale delamination of the lower lithosphere, and small-scale convection around the lithosphere-asthenosphere boundary (Pearce *et al.*, 1990; Keskin, 2003; Omrani *et al.*, 2008; Kaislaniemi *et al.*, 2014). Both slab break-off and wholesale delamination models are inconsistent with the scattered, apparently random nature of the distribution of magmatic centres across the collision zone. The geochemistry of the Mt. Kazbek area lavas is consistent with small-scale convection associated with mantle upwelling as the mechanism for generating the magmatism around Mt. Kazbek and elsewhere in the Greater Caucasus and would explain the chemical variation between volcanic centres.

DATA AVAILABILITY

The data underlying this article are available in the article and in its online supplementary data.

SUPPLEMENTARY DATA

Supplementary data are available at *Journal of Petrology* online.

FUNDING

This work was supported by a PhD studentship funded by the Natural Environment Research Council held by SB (reference NE/K501074/1).

ACKNOWLEDGEMENTS

We thank the three anonymous reviewers for their constructive comments on the manuscript and Georg Zellmer and Tod Waight for their swift handling of the editorial process.

References

Adamia, S. A., Chkhotua, T., Kekelia, M., Lordkipanidze, M., Shavishvili, I. & Zakariadze, G. (1981). Tectonics of the Caucasus and adjoining regions: implications for the evolution of the Tethys Ocean. *Journal of Structural Geology* **3**, 437–447.

Adamia, S., Alania, V., Chabukiani, A., Chichua, G., Enukidze, O. & Sadradze, N. (2010). Evolution of the Late Cenozoic basins of Georgia (SW Caucasus): a review. *Geological Society, London, Special Publications* **340**, 239–259.

Adamia, S., Zakariadze, G., Chkhotua, T., Sadradze, N., Tsereteli, N., Chabukiani, A. & Gventsadze, A. (2011). Geology of the Caucasus: a review. *Turkish Journal of Earth Sciences* **20**, 489–544.

Adamia, S., Alania, V., Tsereteli, N., Varazanashvili, O., Sadradze, N., Lursmanashvili, N. & Gventsadze, A. (2017). Postcollisional tectonics and seismicity of Georgia. Tectonic evolution, collision, and seismicity of Southwest Asia: in honor of Manuel Berberian's forty-five years of research contributions. *Geological Society America Special Paper* **525**, 535–572.

Allen, M. B. & Armstrong, H. A. (2008). Arabia–Eurasia collision and the forcing of mid-Cenozoic global cooling. *Palaeogeography, Palaeoclimatology, Palaeoecology* **265**, 52–58.

Allen, M., Jackson, J. & Walker, R. (2004). Late Cenozoic reorganization of the Arabia–Eurasia collision and the comparison of short-term and long-term deformation rates. *Tectonics* **23**, TC2008. https://doi.org/10.1029/2003TC001530.

Allen, M. B., Morton, A. C., Fanning, C. M., Ismail-Zadeh, A. J. & Kroonenberg, S. B. (2006). Zircon age constraints on sediment provenance in the Caspian region. *Annali di Medicina Straniera* **163**, 647–655.

Allen, M. B., Kheirkhah, M., Neill, I., Emami, M. H. & Mcleod, C. L. (2013). Generation of arc and within-plate chemical signatures in collision zone magmatism: Quaternary lavas from Kurdistan Province, Iran. *Journal of Petrology* **54**, 887–911.

Avdeev, B. & Niemi, N. A. (2011). Rapid Pliocene exhumation of the central Greater Caucasus constrained by low-temperature thermochronometry. *Tectonics* **30**, TC2009. https://doi.org/10.1029/2010TC002808.

Baker, J., Peate, D., Waight, T. & Meyzen, C. (2004). Pb isotopic analysis of standards and samples using a ^{207}Pb–^{204}Pb double spike and thallium to correct for mass bias with a double-focusing MC-ICP-MS. *Chemical Geology* **211**, 275–303.

Bewick, S. (2016) Deciphering the tectonics of the Caucasus from post-collisional volcanism. Ph.D. thesis, Open University (United Kingdom).

Bindeman, I. N., Colon, D. P., Wotzlaw, J. F., Stern, R., Chiaradia, M. & Guillong, M. (2021). Young silicic magmatism of the greater Caucasus, Russia, with implication for its delamination origin based on zircon petrochronology and thermomechanical modeling. *Journal of Volcanology and Geothermal Research* **412**, 107173.

Blundy, J. D., Robinson, J. A. C. & Wood, B. J. (1998). Heavy REE are compatible in clinopyroxene on the spinel lherzolite solidus. *Earth and Planetary Science Letters* **160**, 493–504.

Borghini, G., Fumagalli, P. & Rampone, E. (2017, 2017). Partial melting of secondary pyroxenite at 1 and 1.5 GPa, and its role in upwelling heterogeneous mantle. *Contributions to Mineralogy and Petrology* **172**, 70. https://doi.org/10.1007/s00410-017-1387-4.

Brunet, F. F., Korotaev, M. V., Ershov, A. V. & Nikishin, A. M. (2003). The South Caspian Basin: a review of its evolution from subsidence modelling. *Sedimentary Geology* **156**, 119–148.

Chernyshev, I., Lebedev, V., Bubnov, S., Arakelyants, M. & Goltsman, Y. (2002). Isotopic geochronology of Quaternary volcanic eruptions in the Greater Caucasus. *Geochemical International* **40**, 848–852.

Chiu, H. Y., Chung, S. L., Zarrinkoub, M. H., Melkonyan, R., Pang, K. N., Lee, H. Y., Wang, K. L., Mohammadi, S. S. & Khatib, M. M. (2017). Zircon Hf isotopic constraints on magmatic and tectonic evolution in Iran: implications for crustal growth in the Tethyan orogenic belt. *Journal of Asian Earth Sciences* **145**, 652–669.

Chugaev, A. V., Chernyshev, I. V., Lebedev, V. A. & Eremina, A. V. (2013). Lead isotope composition and origin of the Quaternary lavas of

Elbrus Volcano, the Greater Caucasus: high-precision MC-ICP-MS data. *Petrology* **21**, 16–27.

Cowgill, E., Forte, A. M., Niemi, N., Avdeev, B., Tye, A., Trexler, C., Javakhishvili, Z., Elashvili, M. & Godoladze, T. (2016). Relict basin closure and crustal shortening budgets during continental collision: an example from Caucasus sediment provenance. *Tectonics* **35**, 2918–2947.

Davidson, J., Turner, S., Handley, H., Macpherson, C. & Dosseto, A. (2007). Amphibole 'sponge' in arc crust? *Geology* **35**, 787–790.

Davidson, J., Turner, S. & Plank, T. (2013). Dy/Dy∗: variations arising from mantle sources and petrogenetic processes. *Journal of Petrology* **54**, 525–537.

De Laeter, J. R., Bohlke, J. K., de Bievre, P., Hidaka, H., Peiser, H. S., Rosman, K. J. R. & Taylor, P. D. P. (2003). Atomic weights of the elements. Review 2000 (IUPAC technical report). *Pure and Applied Chemistry* **75**, 683–800.

DePaolo, D. J. (1981). Trace element and isotopic effects of combined wallrock assimilation and fractional crystallization. *Earth and Planetary Science Letters* **53**, 189–202.

Dercourt, J., Zonenshain, L. P., Ricou, L. E., Kazmin, V. G., Le Pichon, X., Knipper, A. L., Grandjacquet, C., Sbortshikov, I. M., Geyssant, J., Lepvrier, C. & Pechersky, D. H. (1986). Geological evolution of the Tethys belt from the Atlantic to the Pamirs since the Lias. *Tectonophysics* **123**, 241–315.

Dzotsenidze, N. (1970). Geology of the Keli volcanic highland. *Proceedings of Geological Institute of Academy of Sciences of GSSR*, new series. **32**, 1–126.

Elliott, T. (2003) Tracers of the slab. In: (Eiler J. (ed)) *Inside the Subduction Factory*. American Geophysical Union, pp.23–45.

Ershov, A. V., Brunet, M.-F., Nikishin, A. M., Bolotov, S. N., Nazarevich, B. P. & Korotaev, M. V. (2003). Northern Caucasus basin: thermal history and synthesis of subsidence models. *Sedimentary Geology* **156**, 95–118.

Forte, A. M., Cowgill, E. & Whipple, K. X. (2014). Transition from a singly vergent to doubly vergent wedge in a young orogen: The Greater Caucasus. *Tectonics* **33**, 2077–2101.

Freeburn, R., Bouilhol, P., Maunder, B., Magni, V. & Van Hunen, J. (2017). Numerical models of the magmatic processes induced by slab breakoff. *Earth and Planetary Science Letters* **478**, 203–213.

Guo, Z. & Wilson, M. (2019). Late Oligocene-early Miocene transformation of post-collisional magmatism in Tibet. *Geology* **47**, 776–780.

Gurbanov, A. G., Gazeev, V. M., Bogatikov, O. A., Naumov, V. B., Dokuchaev, A. Y. & Shevchenko, A. V. (2004). Elbrus active volcano and its geological history. *Russian Journal of Earth Sciences* **6**, 257–277.

Hart, S. R. (1984). A large-scale isotope anomaly in the Southern Hemisphere mantle. *Nature* **309**, 753–757.

Hatzfeld, D. & Molnar, P. (2010). Comparisons of the kinematics and deep structures of the Zagros and Himalaya and of the Iranian and Tibetan plateaus and geodynamic implications. *Reviews. Geophysics* **48**.

Hauri, E.H. & Hart, S.R. (1994). Constraints on melt migration from mantle plumes: a trace element study of peridotite xenoliths from Savai'i, Western Samoa. *Journal of Geophysical Research* **99**, 24301–24321.

Hermann, J. & Rubatto, D. (2009). Accessory phase control on the trace element signature of sediment melts in subduction zones. *Chemical Geology* **265**, 512–526.

Hermann, J., Spandler, C., Hack, A. & Korsakov, A. V. (2006). Aqueous fluids and hydrous melts in high-pressure and ultra-high pressure rocks: implications for element transfer in subduction zones. *Lithos* **92**, 399–417.

Hildreth, W. & Moorbath, S. (1988). Crustal contributions to arc magmatism in the Andes of central Chile. *Contributions to Mineralogy and Petrology* **98**, 455–489.

Hunt, A. C., Parkinson, I. J., Harris, N. B. W., Barry, T. L., Rogers, N. W. & Yondon, M. (2012). Cenozoic volcanism on the Hangai dome, central Mongolia: geochemical evidence for changing melt sources and implications for mechanisms of melting. *Journal of Petrology* **53**, 1913–1942.

Ismail-Zadeh, A., Adamia, S., Chabukiani, A., Chelidze, T., Cloetingh, S., Floyd, M., Gorshkov, A., Gvishiani, A., Ismail-Zadeh, T., Kaban, M. K. & Kadirov, F. (2020). Geodynamics, seismicity, and seismic hazards of the Caucasus. *Earth Sci Rev* **207**.

Jackson, J. & McKenzie, D. (1984). Active tectonics of the Alpine-Himalayan belt between western Turkey and Pakistan. *Geophysical Journal International* **77**, 185–264.

Kaislaniemi, L., van Hunen, J., Allen, M. B. & Neill, I. (2014). Sublithospheric small-scale convection—a mechanism for collision zone magmatism. *Geology* **42**, 291–294.

Keskin (2003). Magma generation by slab steepening and breakoff beneath a subduction-accretion complex: an alternative model for collision-related volcanism in Eastern Anatolia, Turkey. *Geophysical Research Letters* **30**, 8046.

Keskin, M., Pearce, J. A. & Mitchell, J. G. (1998). Volcano-stratigraphy and geochemistry of collision-related volcanism on the Erzurum–Kars Plateau, northeastern Turkey. *Journal of Volcanology and Geothermal Research* **85**, 355–404.

Kessel, R., Schmidt, M. W., Ulmer, P. & Pettke, T. (2005). Trace element signature of subduction-zone fluids, melts and supercritical liquids at 120–180 km depth. *Nature* **437**, 724–727.

Klaver, M., Lewis, J., Parkinson, I. J., Elburg, M. A., Vroon, P. Z., Kelley, K. A. & Elliott, T. (2020). Sr isotopes in arcs revisited: tracking slab dehydration using $\delta^{88/86}$Sr and ^{87}Sr/^{86}Sr systematics of arc lavas. *Geochimica et Cosmochimica Acta* **288**, 101–119.

Koshnaw, R. I., Stockli, D. F. & Schlunegger, F. (2019). Timing of the Arabia–Eurasia continental collision: evidence from detrital zircon U-Pb geochronology of the red bed series strata of the northwest Zagros hinterland, Kurdistan region of Iraq. *Geology* **47**, 47–50.

Koulakov, I., Zabelina, I., Amanatashvili, I. & Meskhia, V. (2012). Nature of orogenesis and volcanism in the Caucasus region based on results of regional tomography. *Solid Earth* **3**, 327–337.

Law, R. & Allen, M. B. (2020). Diachronous Tibetan Plateau landscape evolution derived from lava field geomorphology. *Geology* **48**, 263–267.

Le Bas, M. J., Maitre, R. W. L. E. & Streckeisen, A. (1986). A chemical classification of volcanic rocks based on the total alkali–silica diagram. *Journal of Petrology* **27**, 745–750.

Lebedev, V. A. & Vashakidze, G. T. (2014). The catalogue of Quaternary volcanoes of the Greater Caucasus based on geochronological, volcanological and isotope-geochemical data. *Journal of Volcanology and Seismology* **8**, 93–107.

Lebedev, V. A., Chernyshev, I. V., Chugaev, A. V. & Vashakidze, G. T. (2007). Geochronology of Quaternary volcanism of the Krestovyi Pass Region, Kazbek Neovolcanic Area, Greater Caucasus. *Doklady Earth Sciences* **413**, 272–276.

Lebedev, V. A., Vashakidze, G. T. & Sakhno, V. G. (2008). Potential volcanic danger in the Keli highland (Greater Caucasus): evidence from isotopic-geochronological study of the youngest lavas. *Doklady Earth Sciences* **418**, 169–173.

Lebedev, V. A., Chernyshev, I. V., Chugaev, A. V., Goltsman, Y. V. & Bairova, E. D. (2010). Geochronology of eruptions and parental magma sources of Elbrus volcano, the Greater Caucasus: K–Ar and Sr–Nd–Pb isotope data. *Geochemistry International* **48**, 41–67.

Lebedev, V., Chernyshev, I., Vashakidze, G., Gudina, M. & Yakushev, A. (2012). Geochronology of Miocene volcanism in the northern part of the lesser Caucasus (Erusheti Highland, Georgia). *Doklady Earth Sciences* **444**, 585–590.

Lebedev, V. A., Parfenov, A. V., Vashakidze, G. T., Chernyshev, I. V. & Gabarashvili, Q. A. (2014). Major events in evolution of the Kazbek neovolcanic center, Greater Caucasus: isotope-geochronological data. *Doklady Earth Sciences* **458**, 1092–1098.

Macdonald, G. A. & Katsura, T. (1964). Chemical composition of Hawaiian lavas. *Journal of Petrology* **5**, 82–133.

Mederer, J., Moritz, R., Ulianov, A. & Chiaradia, M. (2013). Middle Jurassic to Cenozoic evolution of arc magmatism during Neotethys subduction and arc-continent collision in the Kapan Zone, southern Armenia. *Lithos* **177**, 61–78.

Mellors, R. J., Jackson, J., Myers, S., Gok, R., Priestley, K., Yetirmishli, G., Turkelli, N. & Godoladze, T. (2012). Deep earthquakes beneath the northern Caucasus: evidence of active or recent subduction in Western Asia. *Bulletin of the Seismological Society of America* **102**, 862–866.

Mibe, K., Kawamoto, T., Matsukage, K. N., Fei, Y. & Ono, S. (2011). Slab melting versus slab dehydration in subduction-zone magmatism. *Proceedings of the National Academy of Sciences* **108**, 8177–8182.

Morton, A., Allen, M., Simmons, M., Spathopoulos, F., Still, J., Hinds, D., Ismail-Zadeh, A. & Kroonenberg, S. (2003). Provenance patterns in a neotectonic basin: Pliocene and Quaternary sediment supply to the South Caspian. *Basin Research* **15**, 321–337.

Mosar, J. O. N., Kangarli, T., Bochud, M., Glasmacher, U. A., Rast, A., Brunet, M.-F., Sosson, M., Institut, U. M. R., Terre, D., Case, P., Azur, C., Albert, R. & Sophia, E. (2010). Cenozoic recent tectonics and uplift in the greater Caucasus: a perspective from Azerbaijan. *Geological Society, London, Special Publications* **340**, 261–280.

Mumladze, T., Forte, A. M., Cowgill, E. S., Trexler, C. C., Niemi, N. A., Yilmaz, M. B. & Kellogg, L. H. (2015). Subducted, detached, and torn slabs beneath the Greater Caucasus. *Geo research journal* **5**, 36–46.

Natal'in, B. A. & Şengör, A. C. (2005). Late Palaeozoic to Triassic evolution of the Turan and Scythian platforms: the pre-history of the Palaeo-Tethyan closure. *Tectonophysics* **404**, 175–202.

Neill, I., Meliksetian, K., Allen, M. B., Navasardyan, G. & Karapetyan, S. (2013). Pliocene–Quaternary volcanic rocks of NW Armenia: magmatism and lithospheric dynamics within an active orogenic plateau. *Lithos* **180–181**, 200–215.

Neill, I., Meliksetian, K., Allen, M. B., Navasardyan, G. & Kuiper, K. (2015). Petrogenesis of mafic collision zone magmatism: the Armenian sector of the Turkish–Iranian plateau. *Chemical Geology* **403**, 24–41.

Nowell, G. M., Pearson, D. G., Ottley, C. J., Schwieters, J. & Dowall, D. (2003) Long-term performance characteristics of a plasma ionisation multi-collector mass spectrometer (PIMMS): the Thermofinnigan Neptune. In: (Tanner S. D. & Holland G. (eds)) *Plasma Source Mass Spectrometry: Applications and Emerging Technologies*. The Royal Society of Chemistry, pp. 307–320.

Okay, A. I., Şengör, A. C. & Görür, N. (1994). Kinematic history of the opening of the Black Sea and its effect on the surrounding regions. *Geology* **22**, 267–270.

Omrani, J., Agard, P., Whitechurch, H., Benoit, M., Prouteau, G. & Jolivet, L. (2008). Arc-magmatism and subduction history beneath the Zagros Mountains, Iran: a new report of adakites and geodynamic consequences. *Lithos* **106**, 380–398.

Palme, H. & O'Neill, H. (2014) Cosmochemical estimates of mantle composition. In: (Holland H. D. & Turekian K. K. (eds)) *Treatise on Geochemistry*. Oxford: Elsevier, pp.1–39.

Parfenov, A. V., Lebedev, V. A., Chernyshev, I. V., Vashakidze, G. T., Yakushev, A. I., Goltsman, Y. V., Chugaev, A. V., Oleinikova, T. I., Kanunnikova, E. M. & Gabarashvili, K. A. (2019). Petrological–geochemical characteristics of lavas, sources and evolution of magmatic melts of the Kazbek Neovolcanic center (Greater Caucasus). *Petrology* **27**, 606–632.

Pearce, J. A., Bender, J., Delong, S. E., Kidd, W. S. F., Low, P. J., Guner, Y., Saroglu, F., Yilmaz, Y., Moorbath, S. & Mitchell, J. (1990). Genesis of collision volcanism in Eastern Anatolia, Turkey. *Journal of Volcanology and Geothermal Research* **44**, 189–229.

Pearce, J. A. & Peate, D. W. (1995). Tectonic implications of the composition of volcanic arc magmas. *Annual Review of Earth and Planetary Sciences* **23**, 251–285.

Pearce, J. A. (2008). Geochemical fingerprinting of oceanic basalts with applications to ophiolite classification and the search for Archean oceanic crust. *Lithos* **100**, 14–48.

Peccerillo, A. & Taylor, S. R. (1976). Geochemistry of Eocene calc-alkaline volcanic rocks from the Kastamonu area, northern Turkey. *Contributions to Mineralogy and Petrology* **58**, 63–81.

Perotti, C., Chiariotti, L., Bresciani, I., Cattaneo, L. & Toscani, G. (2016). Evolution and timing of salt diapirism in the Iranian sector of the Persian Gulf. *Tectonophysics* **679**, 180–198.

Philip, H., Cisternas, A., Gvishiani, A. & Gorshkuv, A. (1989). The Caucasus: an actual example of the initial stages of continental collision. *Tectonophysics* **161**, 1–21.

Pin, C., Gannoun, A. & Duponta, A. (2014). Rapid, simultaneous separation of Sr, Pb, and Nd by extraction chromatography prior to isotope ratios determination by TIMS and MC-ICP-MS. *Journal of Analytical Atomic Spectrometry* **29**, 1858–1870.

Plank, T. (2005). Constraints from thorium/lanthanum on sediment recycling at subduction zones and the evolution of the continents. *Journal of Petrology* **46**, 921–944.

Plank, T. & Langmuir, C. H. (1998). The chemical composition of subducting sediment and its consequences for the crust and mantle. *Chemical Geology* **145**, 325–394.

Prelević, D., Foley, S. F., Romer, R. & Conticelli, S. (2008). Mediterranean tertiary lamproites derived from multiple source components in post-collisional geodynamics. *Geochimica et Cosmochimica Acta* **72**, 2125–2156.

Putirka, K. D. (2008). Thermometers and barometers for volcanic systems. *Reviews in Mineralogy and Geochemistry* **69**, 61–120.

Raczek, I., Jochum, K. P. & Hofmann, A. W. (2003). Neodymium and strontium isotope data for USGS reference materials BCR-1, BCR-2, BHVO-1, BHVO-2, AGV-1, AGV-2, GSP-1, GSP-2 and eight MPI-DING reference glasses. *Geostandards Newsletter* **27**, 173–179.

Ramsey, M. H., Potts, P. J., Webb, P. C., Watkins, P., Watson, J. S. & Coles, B. J. (1995). An objective assessment of analytical method precision: comparison of ICP-AES and XRF for the analysis of silicate rocks. *Chemical Geology* **124**, 1–19.

Reilinger, R., McClusky, S., Vernant, P., Lawrence, S., Ergintav, S., Cakmak, R., Ozener, H., Kadirov, F., Guliev, I., Stepanyan, R., Nadariya, M., Hahubia, G., Mahmoud, S., Sakr, K., ArRajehi, A., Paradissis, D., Al-Aydrus, A., Prilepin, M., Guseva, T., Evren, E., Dmitrotsa, A., Filikov, S. V., Gomez, F., Al-Ghazzi, R. & Karam, G. (2006). GPS constraints on continental deformation in the Africa–Arabia–Eurasia continental collision zone and implications for the dynamics of plate interactions. *Journal of Geophysical Research* **111**, 1–26.

Robinson, J. A. C., Wood, B. J. & Blundy, J. D. (1998). The beginning of melting of fertile and depleted peridotite at 1.5 GPa. *Earth and Planetary Science Letters* **155**, 97–111.

Rogers, N. W., Thomas, L. E., Macdonald, R., Hawkesworth, C. J. & Mokadem, F. (2006). 238U-230Th disequilibrium in recent basalts

and dynamic melting beneath the Kenya rift. *Chemical Geology* **234**, 148–168.

Saintot, A., Brunet, M. F., Yakovlev, F., Sebrier, M., Stephenson, R., Ershov, A., Chalot-Prat, F. & McCann, T. (2006). The Mesozoic-Cenozoic tectonic evolution of the Greater Caucasus. In: Gee, D.G. & Stephenson, R.A. (eds) *Geological Society, London, Memoirs* **32**, 277–289.

Şengör, A. C. (1990). Plate tectonics and orogenic research after 25 years: a Tethyan perspective. *Earth Science Reviews* **27**, 1–201.

Sisson, T. W. (1994). Hornblende-melt trace-element partitioning measured by ion microprobe. *Chemical Geology* **117**, 331–344.

Skora, S. & Blundy, J. (2010). High-pressure hydrous phase relations of radiolarian clay and implications for the involvement of subducted sediment in arc magmatism. *Journal of Petrology* **51**, 2211–2243.

Sokól, K., Halama, R., Meliksetian, K., Savov, I. P., Navasardyan, G. & Sudo, M. (2018). Alkaline magmas in zones of continental convergence: the Tezhsar volcano-intrusive ring complex, Armenia. *Lithos* **320-321**, 172–191.

Sosson, M., Rolland, Y., Mller, C., Danelian, T., Melkonyan, R., Kekelia, S., Adamia, S., Babazadeh, V., Kangarli, T., Avagyan, A., Galoyan, G. & Mosar, J. (2010). Subductions, obduction and collision in the Lesser Caucasus (Armenia, Azerbaijan, Georgia), new insights. *Geological Society, London, Special Publications* **340**, 329–352.

Sosson, M., Stephenson, R. & Adamia, S. (2017). Tectonic evolution of the Eastern Black Sea and Caucasus: an introduction. *Geological Society, London, Special Publications* **428**, 1–9.

Sugden, P. J., Savov, I. P., Wilson, M., Meliksetian, K., Navasardyan, G. & Halama, R. (2019). The thickness of the mantle lithosphere and collision-related volcanism in the Lesser Caucasus. *Journal of Petrology* **60**, 199–230.

Sugden, P. J., Savov, I. P., Agostini, S., Wilson, M., Halama, R. & Meliksetian, K. (2020). Boron isotope insights into the origin of subduction signatures in continent-continent collision zone volcanism. *Earth and Planetary Science Letters* **538**, 116207.

Thirlwall, M. F. (2002). Multicollector ICP-MS analysis of Pb isotopes using a ^{207}Pb–^{204}Pb double spike demonstrates up to 400 ppm/amu systematic errors in Tl-normalization. *Chemical Geology* **184**, 255–279.

Thompson, M., Potts, P. J., Kane, J. S., Webb, P. C. & Watson, J. S. (2000). GeoPT4. An International Proficiency Test for Analytical Geochemistry Laboratories-Report on Round 4 (March 1999). *Geostandards Newsletter* **24**, E1–E37.

Vernant, P., Nilforoushan, F., Hatzfeld, D., Abbassi, M. R., Vigny, C., Masson, F., Nankali, H., Martinod, J., Ashtiani, A., Bayer, R. & Tavakoli, F. (2004). Present-day crustal deformation and plate kinematics in the Middle East constrained by GPS measurements in Iran and northern Oman. *Geophysical Journal International* **157**, 381–398.

Vincent, S. J., Morton, A. C., Carter, A., Gibbs, S. & Barabadze, T. G. (2007). Oligocene uplift of the Western Greater Caucasus: an effect of initial Arabia–Eurasia collision. *Terra Nova* **19**, 160–166.

Vincent, S. J., Saintot, A., Mosar, J., Okay, A. I. & Nikishin, A. M. (2018). Comment on "Relict basin closure and crustal shortening budgets during continental collision: an example from Caucasus sediment provenance" by Cowgill *et al.*, 2016. *Tectonics* **37**, 1006–1016.

Vincent, S. J., Somin, M. L., Carter, A., Vezzoli, G., Fox, M. & Vautravers, B. (2020). Testing models of Cenozoic exhumation in the western Greater Caucasus. *Tectonics* **39**, e2018TC005451. https://doi.org/10.1029/2018TC005451.

Weis, D., Kieffer, B., Maerschalk, C., Barling, J., De Jong, J., Williams, G. A., Hanano, D., Pretorius, W., Mattielli, N., Scoates, J. S., Goolaerts, A., Friedman, R. M. & Mahoney, J. B. (2006). High-precision isotopic characterization of USGS reference materials by TIMS and MC-ICP-MS. *Geochemistry, Geophysics, Geosystems*(8) **7**.

Workman, R. K. & Hart, S. R. (2005). Major and trace element composition of the depleted MORB mantle (DMM). *Earth and Planetary Science Letters* **231**, 53–72.

Wood, B. J. & Blundy, J. D. (1997). A predictive model for rare earth element partitioning between clinopyroxene and anhydrous silicate melt. *Contributions to Mineralogy and Petrology* **129**, 166–181.

Wood, B. J. & Blundy, J. D. (2003). Trace element partitioning under crustal and uppermost mantle Conditions: the influences of ionic radius, cation charge, pressure, and temperature, *Treatise on Geochemistry* **2**, 395–424.

Zabelina, I., Koulakov, I., Amanatashvili, I., El Khrepy, S. & Al-Arifi, N. (2016). Seismic structure of the crust and uppermost mantle beneath Caucasus based on regional earthquake tomography. *Journal of Asian Earth Sciences* **119**, 87–99.

Zindler, A. & Hart, S. R. (1986). Chemical Geodynamics. *Annual Review of Earth and Planetary Sciences* **14**, 493–571.